



This is a repository copy of *GaAs/Al_{0.8}Ga_{0.2}As separate absorption and multiplication region x-ray spectroscopic avalanche photodiodes*.

White Rose Research Online URL for this paper:
<http://eprints.whiterose.ac.uk/166995/>

Version: Accepted Version

Article:

Whitaker, M.D.C., Lioliou, G., Krysa, A.B. orcid.org/0000-0001-8320-7354 et al. (1 more author) (2020) GaAs/Al_{0.8}Ga_{0.2}As separate absorption and multiplication region x-ray spectroscopic avalanche photodiodes. *Journal of Applied Physics*, 128 (1). 015704. ISSN 0021-8979

<https://doi.org/10.1063/5.0009830>

This article may be downloaded for personal use only. Any other use requires prior permission of the author and AIP Publishing. This article appeared in M. D. C. Whitaker, G. Lioliou, A. B. Krysa, and A. M. Barnett, GaAs/Al_{0.8}Ga_{0.2}As separate absorption and multiplication region x-ray spectroscopic avalanche photodiodes, *Journal of Applied Physics* 128:1, 015704, and may be found at <https://doi.org/10.1063/5.0009830>

Reuse

Items deposited in White Rose Research Online are protected by copyright, with all rights reserved unless indicated otherwise. They may be downloaded and/or printed for private study, or other acts as permitted by national copyright laws. The publisher or other rights holders may allow further reproduction and re-use of the full text version. This is indicated by the licence information on the White Rose Research Online record for the item.

Takedown

If you consider content in White Rose Research Online to be in breach of UK law, please notify us by emailing eprints@whiterose.ac.uk including the URL of the record and the reason for the withdrawal request.



eprints@whiterose.ac.uk
<https://eprints.whiterose.ac.uk/>

1 GaAs/Al_{0.8}Ga_{0.2}As Separate Absorption and Multiplication Region X-ray 2 Spectroscopic Avalanche Photodiodes

3 M.D.C. Whitaker^{1*}, G. Lioliou¹, A.B. Krysa², and A.M. Barnett¹

4 ¹Space Research Group, Sch. of Engineering and Informatics, University of Sussex, Falmer, Brighton, BN1 9QT, UK

5 ²National Epitaxy Facility, University of Sheffield, Mappin Street, Sheffield, S1 3JD, UK

6
7 A GaAs/Al_{0.8}Ga_{0.2}As Separate Absorption and Multiplication (SAM) X-ray avalanche photodiode (APD)
8 structure was grown by metalorganic vapour phase epitaxy. Mesa photodiodes of different diameter (200 μm and
9 400 μm) were fabricated from the structure. Two of the photodiodes (one of each diameter) were characterised
10 at 20 °C for their electrical properties and response to X-rays using an ⁵⁵Fe radioisotope X-ray (Mn K α = 5.9 keV;
11 Mn K β = 6.49 keV) source. An energy resolution of 508 eV \pm 5 eV Full Width at Half Maximum (FWHM) at
12 5.9 keV was achieved at an apparent avalanche gain, M, of 1.1. This is the best energy resolution so far reported
13 for GaAs/Al_xGa_{1-x}As X-ray SAM APDs. The noise components associated with the achievable spectroscopic
14 energy resolutions are reported. Comparisons between the 200 μm and 400 μm diameter GaAs/Al_xGa_{1-x}As SAM
15 X-ray APDs and recently studied GaAs p⁺-i-n⁺ detectors were made, showing that the inclusion of the avalanche
16 layer improves the achievable energy resolution; energy resolutions of 508 eV FWHM at 5.9 keV at M = 1.1 and
17 603 eV FWHM at 5.9 keV at M = 1.2 were achieved with the 200 μm and 400 μm diameter GaAs/Al_xGa_{1-x}As
18 SAM X-ray APDs respectively; this is better than was previously reported for similar devices without avalanche
19 layers: 690 eV FWHM at 5.9 keV and 730 eV FWHM at 5.9 keV for 200 μm and 400 μm diameter GaAs p⁺-i-n⁺
20 detectors respectively (G.Lioliou et al., J. Appl. Phys. 122, 244506 (2017)).

21 22 KEYWORDS

23 GaAs; AlGaAs; SAM; APD; X-ray detector; Spectroscopy

24 25 I. INTRODUCTION

26 Due to the limitations of narrow bandgap (typically Si) X-ray spectrometers commonly in use today [1, 2], a
27 variety of wide bandgap materials, such as GaAs [3-7], diamond [8, 9], SiC [10-12], In_{0.5}Ga_{0.5}P [13, 14],
28 Al_{0.52}In_{0.48}P [15-17], and Al_xGa_{1-x}As [18-21], have been investigated as potential X-ray detector
29 replacements. The cooling systems and radiation shielding often required for Si X-ray spectrometers [22] place
30 substantial burdens on spacecraft mass, volume, and power consumption, limiting their suitability for certain space
31 science applications (e.g. missions to study the surface of Mercury, or the Jovian moons, where temperatures
32 and/or radiation intensities are significant). Wide bandgap materials, such as GaAs and Al_xGa_{1-x}As, offer an
33 alternative. Such materials can operate in a large range of thermal and radiation environments, while still
34 providing sub-keV spectral resolutions at soft X-ray energies [22]. In the case of GaAs, its wider bandgap
35 (1.43 eV for GaAs cf. 1.12 eV for Si [22]), larger X-ray absorption coefficient (837 cm⁻¹ for GaAs cf. 346 cm⁻¹
36 for Si, at 5.9 keV [23]), and improved radiation hardness in comparison to Si [24], allows for superior energy
37 resolutions at high temperature [25], thinner X-ray detecting structures [26], and potentially longer instrument
38 lifetimes in intense radiation environments.

*Corresponding author, E-mail address: M.Whitaker@sussex.ac.uk

39
40
41
42
43
44
45
46
47
48
49
50
51
52
53
54
55
56
57
58
59
60
61
62
63
64
65
66
67
68
69
70
71
72
73
74
75
76
77
78

Various prototype GaAs based X-ray spectrometers have been reported, with most work focused on GaAs p⁺-i-n⁺ mesa X-ray photodiodes operated in the non-avalanche regime. Circular mesa GaAs, 200 μm diameter, 7 μm thick i layer, p⁺-i-n⁺ photodiodes have been characterised across the temperature range 60 °C to 0 °C, with an energy resolution of 750 eV FWHM at 5.9 keV for the best performing device at 20 °C [6]. Similar GaAs photodiodes (10 μm i layer) have been characterised over the temperature range 100 °C to -20 °C, with an energy resolution of 690 eV FWHM at 5.9 keV reported at room temperature (20 °C) [27]. GaAs planar p⁺-i-n⁺ photodiode arrays have also been reported with very promising results; a 5 × 5 pixel, 40 μm i layer, GaAs p⁺-i-n⁺ diode array structure had a reported energy resolution of 266 eV FWHM at 5.9 keV at room temperature [3]. GaAs arrays of a similar structure, but with thicker epilayer layers (325 μm i layer), had a reported energy resolution of 300 eV FWHM at 5.9 keV at room temperature [28].

Al_xGa_{1-x}As, due to the material's ability to be tailored to particular application environments by adjusting the Al fraction (e.g. a reduction in Al fraction reduces the bandgap), has gained attention as an interesting material for X-ray detection [21, 26, 29]. Most work has focused on Al_xGa_{1-x}As p⁺-i-n⁺ mesa photodiodes, operated within the non-avalanche regime. Circular mesa Al_{0.8}Ga_{0.2}As, 200 μm diameter, 1 μm i layer, p⁺-i-n⁺ photodiodes have been characterised across the temperature range 90 °C to -30°C, with an energy resolution of 1.07 keV FWHM at 5.9 keV reported at 20 °C [29]. Circular mesa Al_{0.2}Ga_{0.8}As, 200 μm diameter, 3 μm i layer, p⁺-i-n⁺ photodiodes have been characterised across the temperature range 20 °C to -20 °C, with an energy resolution of 1.06 keV FWHM at 5.9 keV reported at 20 °C [21]. A 2 × 2 square pixel Al_{0.2}Ga_{0.8}As array (each photodiode area 200 μm by 200 μm, 3 μm i layer) was also recently reported with improved results; an energy resolution of 760 eV FWHM at 5.9 keV at 20 °C was achieved [26].

Whilst non-avalanche GaAs and Al_xGa_{1-x}As X-ray detectors show great promise, the demands they place on their preamplifier electronics are more stringent than those of narrower bandgap materials like Si, because the electron-hole pair creation energies of GaAs and Al_xGa_{1-x}As are larger (e.g. 4.2 eV for GaAs cf. 3.6 eV for Si [22]). Avalanche photodiodes (APDs) potentially reduce those demands by increasing the amount of charge created from the absorption of an X-ray photon. However, the greater operating biases required can cause higher leakage currents which results in more parallel white noise.

APDs are widely used in photonic detection systems, most notably within telecommunications [30-33], to improve response relative to that of conventional p⁺-i-n⁺ photodiodes [30]. The increased response from such APDs is due to the impact ionisation process, where charge carriers gain enough kinetic energy to generate electron-hole pairs during collisions with atoms in the lattice [34, 35].

For photons of infrared to ultraviolet wavelength, where the photon energy is of the same order as the bandgap energy of the detector material, the stochastic nature of the impact ionisation process in APDs commonly adds noises (quantified by the so called the excess noise factor, N_x) to the signal [36, 37] such that

$$N_x = kM + \left(2 - \frac{1}{M}\right)(1 - k), \quad (1)$$

79
80
81
82
83
84
85
86
87
88
89
90
91
92
93
94
95
96
97
98
99
100
101
102
103
104
105
106
107
108
109
110
111
112
113
114
115
116
117

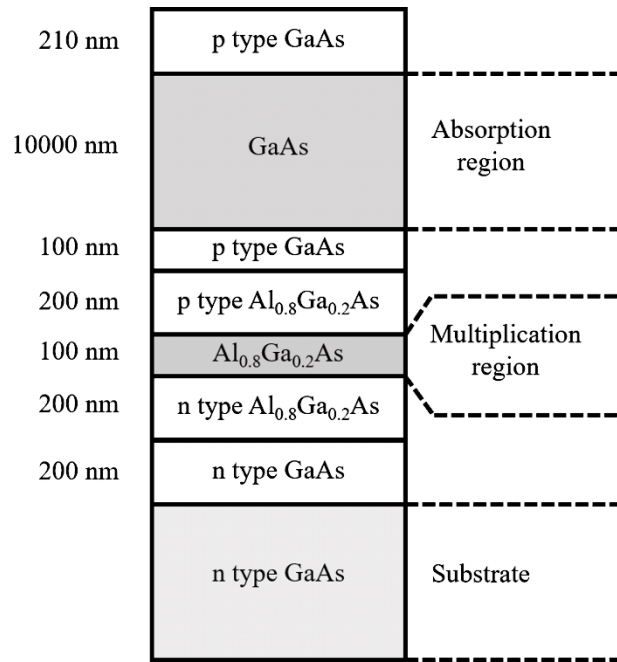
where $k (= \beta/\alpha)$ is the ratio between the hole (β) and electron (α) ionisation coefficients, which represent the inverse of the mean distance between successive impact ionisation events [36]. In most compound semiconductors, k can range from 0.3 to 1.0, leading to a large N_x [38]. Hence, as per Eq. 1, assuming an extension of applicability of this model to the X-ray case, a poor energy resolution was originally expected [38]. For this reason, it was originally thought that the use of APDs would degrade the resolution of X-ray spectrometers and hence they were not extensively investigated [39]. However, recent studies have improved the understanding of APDs [31, 35, 36, 38, 40]. Notably, Tan et al. [38] showed that the common model of excess noise is not directly applicable at X-ray energies, since the distribution of avalanche gains tightens as the initiating photon energy, E , is increased, thus leading to significantly lower additional noise for X-rays than would be expected in the case for infrared, visible, or UV photons [38]. Additional design choices such as using very thin avalanche layers can also be used to reduce excess noise [31].

The first X-ray APDs were complex staircase band structures [18, 41, 42]. For example, a GaAs/ $\text{Al}_x\text{Ga}_{1-x}\text{As}$ SAM APD ($320 \mu\text{m} \times 450 \mu\text{m}$ active area) was reported to function as an X-ray detector at room temperature, utilising a series of staircase multiplication regions [18]; an energy resolution of 900 eV FWHM at 13.96 keV was reported at an avalanche multiplication of 4.1 at room temperature [18]. More recent work has concentrated on simpler SAM APD structures [43]. For example, a thin (430 nm GaAs absorption layer, 220 nm $\text{Al}_{0.8}\text{Ga}_{0.2}\text{As}$ multiplication layer) GaAs/ $\text{Al}_{0.8}\text{Ga}_{0.2}\text{As}$ SAM X-ray APD was reported at room temperature [44]; it had an energy resolution of 1.08 keV FWHM at 5.9 keV, at an avalanche multiplication of 3.5.

In this work we report the growth, fabrication, and characterisation at room temperature (20 °C) of two new circular GaAs/ $\text{Al}_{0.8}\text{Ga}_{0.2}\text{As}$ SAM X-ray photodiodes of different diameter (200 μm and 400 μm). The results are compared with recently reported non-avalanche GaAs $\text{p}^+\text{-i-n}^+$ X-ray photodiodes of the same size (200 μm and 400 μm diameter) and with the same absorption layer thickness (10 μm) [27]. The same measurement techniques and readout electronics were used in both cases. The work shows that the addition of the avalanche layer improves the energy resolution. This unambiguous comparison of the detectors both with and without an avalanche layer but otherwise of the same design provides conclusive evidence that the addition of an avalanche layer can be used to improve the energy resolution of a spectroscopic photon counting X-ray detector.

II. DIODE DESIGN

The GaAs/ $\text{Al}_{0.8}\text{Ga}_{0.2}\text{As}$ SAM structure (see Fig. 1) was grown by metalorganic vapour phase epitaxy upon a commercial GaAs n^+ substrate. The photodiode layer details are outlined in Table 1. Circular mesa structures of 200 μm diameter and 400 μm diameter were etched using a 1:1:1 $\text{H}_3\text{PO}_4\text{:H}_2\text{O}_2\text{:H}_2\text{O}$ solution followed by 10 s in a 1:8:80 $\text{H}_2\text{SO}_4\text{:H}_2\text{O}_2\text{:H}_2\text{O}$ solution. Ohmic contacts consisting of 200 nm Au and 20 nm Ti were evaporated upon the top p^+ side of the mesa structures and ohmic contacts consisting of 200 nm Au and 20 nm InGe were evaporated upon the back side of the substrate. The top contacts covered 45% of the 200 μm diameter diode's face and 33% of the 400 μm diameter diode's face.



118

119 Fig. 1. Schematic of GaAs/Al_{0.8}Ga_{0.2}As SAM structure.

120

121 Table 1. GaAs/Al_{0.8}Ga_{0.2}As SAM layer details.

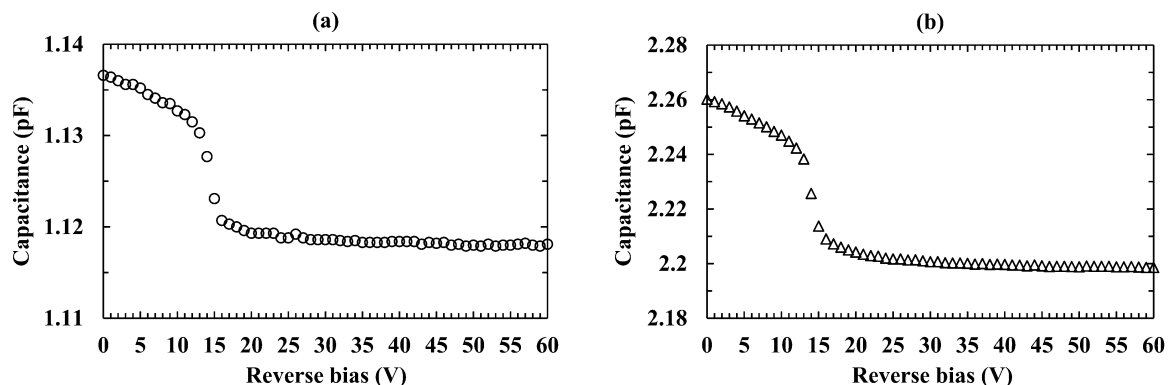
Material	Dopant	Dopant type	Thickness (nm)	Doping density (cm ⁻³)
GaAs	Zn	p	10	1×10 ¹⁹
GaAs	Zn	p	200	2×10 ¹⁸
GaAs			10000	Undoped
GaAs	Zn	p	100	2×10 ¹⁷
Al _{0.8} Ga _{0.2} As	Zn	p	200	2×10 ¹⁷
Al _{0.8} Ga _{0.2} As			100	Undoped
Al _{0.8} Ga _{0.2} As	Si	n	200	2×10 ¹⁸
GaAs	Si	n	200	2×10 ¹⁸
GaAs n ⁺ substrate				

122

123 **III. DETECTOR ELECTRICAL CHARACTERISATION**124 **A. Capacitance as a function of applied reverse bias**

125 For each GaAs/Al_{0.8}Ga_{0.2}As SAM photodiode (200 μm and 400 μm diameter), capacitance as a function of reverse
 126 bias, V_R, was measured using an HP 4275A LCR Meter (50 mV rms signal magnitude; 1 MHz frequency). A
 127 Keithley 6487 voltage source/picoammeter was used to bias the detectors. Each device was placed within a
 128 custom-made, light-tight, electromagnetically screened test fixture and, for temperature control, inserted in a TAS
 129 Micro MT environmental chamber. An appropriately positioned thermocouple was used to ensure thermal
 130 equilibrium (20 °C) was reached between the environmental chamber and the devices. The test fixture and
 131 environmental chamber were purged with dry N₂ (<5% relative humidity) in order to remove any humidity related
 132 effects [6]. The environmental chamber was set to 20 °C and left for 1 hour before measuring to ensure thermal

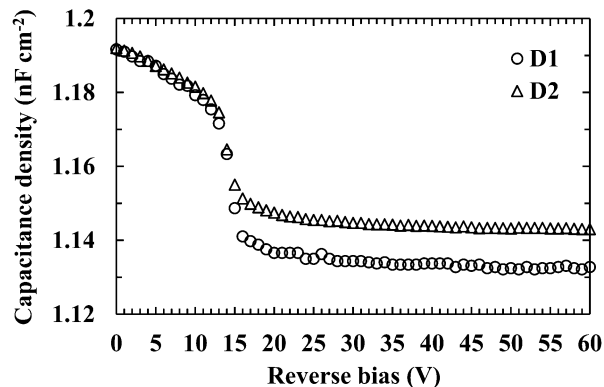
133 equilibrium. The measured capacitances as functions of reverse bias for (a) the 200 μm diameter device and (b)
134 the 400 μm diameter device is shown in Fig. 2.
135



136
137 Fig. 2. Capacitance for (a) the 200 μm diameter device and (b) the 400 μm diameter device, as a function of applied reverse
138 bias, at 20 $^{\circ}\text{C}$. The empty package capacitance, in each case, has not been subtracted.
139

140 The measured capacitance of both packaged devices decreased with increasing reverse bias, from 1.14 pF and
141 2.26 pF at $V_R = 0$ V for the 200 μm and 400 μm diameter device respectively, to 1.12 pF and 2.20 pF at $V_R = 60$ V
142 for the 200 μm and 400 μm diameter device respectively. The uncertainty associated with each individual
143 capacitance measurement was $\approx \pm 0.03$ pF. However, because a set of measurements were taken without
144 modifying the conditions (e.g. no variations in electrical connections and temperature), fittings on the
145 experimental data provide a more appropriate uncertainty for relative changes [45]. Exponential fittings on the
146 measured capacitance for each device were performed as a function of reverse bias. An uncertainty of ± 0.4 fF
147 was estimated. The drop in capacitance across both the 200 μm and 400 μm diameter devices, within the range
148 $13 \text{ V} \leq V_R \leq 16 \text{ V}$, indicated that the punch-through voltage (the voltage at which the multiplication region rapidly
149 depletes) was ≈ 14 V [44].

150
151 The measured capacitance, C_M , included both the diode capacitance, C_D , and the package capacitance, C_P , since
152 the devices were packaged. C_P was removed by assuming a constant capacitance density as a function of device
153 area. The capacitance density of the 200 μm diameter device and the 400 μm diameter device at each applied
154 reverse bias were compared, and the empty package capacitance calculated. A mean average empty package
155 capacitance (0.76 pF) was calculated for C_P and was subsequently subtracted from C_M for each device. Fig. 3
156 presents the capacitance densities for the 200 μm and 400 μm diameter devices.
157



158

159

Fig. 3. Capacitance density for the 400 μm diameter device (triangles) and the 200 μm diameter device (circles) as a function of applied reverse bias, at 20 $^{\circ}\text{C}$, taking into account the empty package capacitance (0.76 pF).

160

161

162

The capacitances of the devices were defined primarily by the depletion layer capacitance, C_{DL} of each device [34]. Therefore, the depletion width, W , could be calculated using the equation

163

164

165

$$W = \frac{\epsilon_0 \epsilon A}{C_{DL}}, \quad (2)$$

166

167

where A is the device area, ϵ is the relative permittivity of the material, and ϵ_0 is the permittivity of free space [34].

168

169

170

171

172

For the reported devices, multiple materials (GaAs and $\text{Al}_{0.8}\text{Ga}_{0.2}\text{As}$) influence C_{DL} , with their associated contributions difficult to detangle. As such, in order to calculate W , the devices were approximated to be simple GaAs structures ($\epsilon = 13.16$ [46]). Since ϵ of $\text{Al}_{0.8}\text{Ga}_{0.2}\text{As}$ ($= 10.628$ [47]) is smaller in value, the presently reported W should be taken as an upper limit. The Debye length of GaAs (0.06 μm) was also taken into account when calculating the depletion width uncertainty [48]. Fig. 4 (a) shows the depletion width as a function of applied reverse bias.

173

174

175

176

177

178

179

The depletion width increased as a function of applied reverse bias for both devices, increasing from 9.8 $\mu\text{m} \pm 0.1 \mu\text{m}$ at $V_R = 0 \text{ V}$ for the 200 μm and 400 μm diameter device, to 10.3 $\mu\text{m} \pm 0.1 \mu\text{m}$ and 10.2 $\mu\text{m} \pm 0.1 \mu\text{m}$ at $V_R = 60 \text{ V}$ for the 200 μm and 400 μm diameter device, respectively. As was the case in Fig. 2, the increase in depletion width across both the 200 μm and 400 μm diameter devices, between 13 V and 16 V, indicated the punch-through voltage. Linear least squares fitting was applied to both devices, and indicated that the devices were fully depleted at $V_R \geq 50 \text{ V}$.

180

181

182

183

184

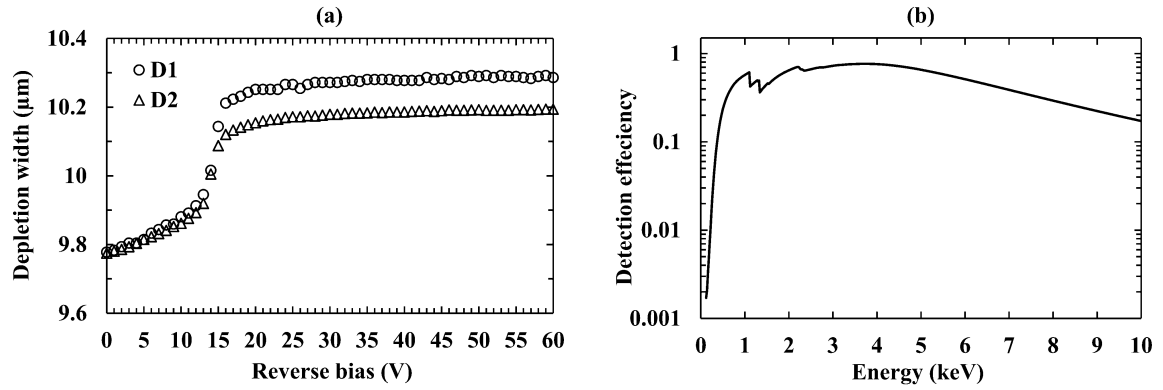
185

186

187

The GaAs/ $\text{Al}_{0.8}\text{Ga}_{0.2}\text{As}$ SAM APD structure quantum detection efficiency was calculated using the Beer-Lambert law, assuming that the active region was solely confined to the GaAs absorption layer and that it was fully depleted and active. The results can be seen in Fig. 4 (b). For photons of 5.9 keV energy, the quantum detection efficiencies of the devices structure presented here were 0.56 in areas not covered by the top contact, and 0.46 in areas covered by the top contact. The weighted quantum efficiency assuming uniform illumination of the devices was 0.52 and 0.53 for the 200 μm and 400 μm diameter detectors, respectively.

188



189

190

191

192

193

194

195

196

197

198

199

200

201

202

203

204

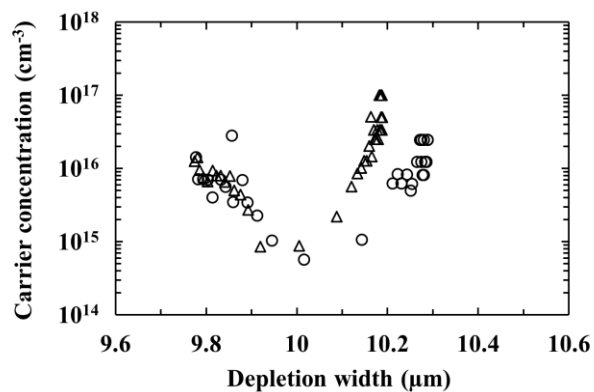
205

Fig. 4. (a) Calculated depletion width for the 200 μm diameter device (circles) and the 400 μm diameter device (triangles) as a function of applied reverse bias, at 20 $^{\circ}\text{C}$. (b) Calculated detection efficiency for the GaAs/Al_{0.8}Ga_{0.2}As SAM APD structure as a function of energy. The Al K, Ga L, and As L X-ray absorption edges are responsible for the detection efficiency discontinuities.

The general nonuniform distributions equation [34] was used to calculate the carrier concentration of the space charge region, N , where,

$$\frac{d(1/C_{DL}^2)}{dV_R} = \frac{2}{q\epsilon_0\epsilon N}, \quad (3)$$

where q is the elementary charge and the other symbols have previously been defined. For both devices, at a calculated depletion width $\approx 10 \mu\text{m}$, the carrier concentration reached a minimum of $\approx 7 \times 10^{14} \text{ cm}^{-3}$. Fig. 5 presents the carrier concentration for the GaAs/Al_{0.8}Ga_{0.2}As detectors as a function of calculated depletion width. Variation in the apparent carrier concentration between the 200 μm and 400 μm devices was within the uncertainty of the measurements.



206

207

208

209

210

Fig. 5. Carrier concentration for the 200 μm (circles) and 400 μm (triangles) diameter devices as a function of calculated depletion width.

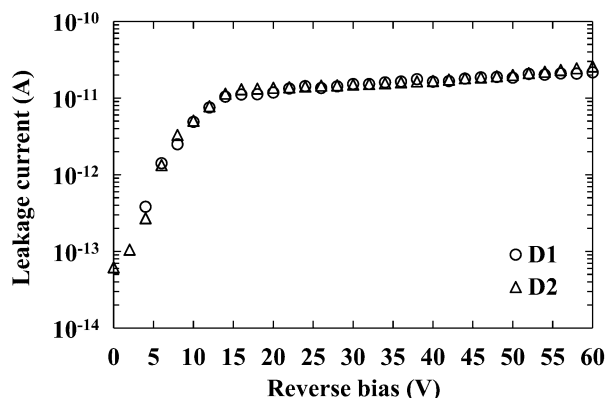
B. Current as a function of applied reverse bias

211

212

The leakage current of the 200 μm and 400 μm diameter devices was measured using a Keithley 6487 voltage source/picoammeter as a function of applied reverse bias. The environmental conditions were the same as for the

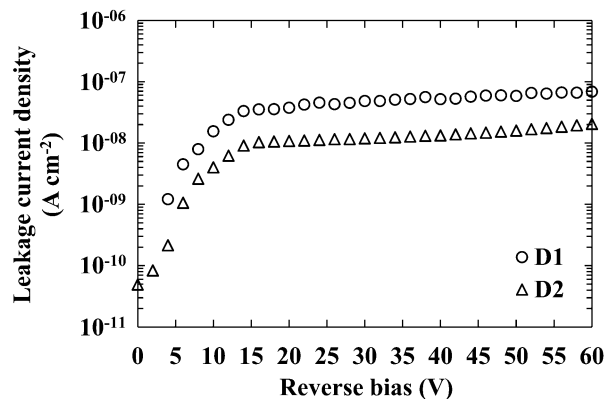
213 capacitance measurements. Fig. 6 presents the measured leakage current, I_R , of the packaged devices as a function
 214 of applied reverse bias.
 215



216
 217 Fig. 6. Leakage current for the 200 μm diameter device (circles) and the 400 μm diameter device (triangles) as a function of
 218 applied reverse bias.
 219

220 For both packaged devices, the leakage current increased with increasing reverse bias. At the maximum applied
 221 reverse bias (60 V), the leakage currents were measured to be $21.6 \text{ pA} \pm 0.8 \text{ pA}$ for the 200 μm device and 25.7 pA
 222 $\pm 0.5 \text{ pA}$ for the 400 μm device. The uncertainties associated with the current measurements were dominated by
 223 the uncertainty associated with a single measurement from the Keithley 6487 voltage source/picoammeter.
 224

225 In order to determine the corresponding leakage current density, J_R , of the devices, the leakage current associated
 226 with the package (and measurement system) was determined by measuring an empty package of identical type.
 227 It was found that the empty package's leakage current was smaller than the uncertainty ($\pm 0.4 \text{ pA}$) of the
 228 instrument, it was therefore considered negligible. The apparent leakage current density, as shown in Fig. 7, of
 229 the 400 μm diameter device was improved (lower) relative to the 200 μm diameter device (20.4 nA cm^{-2}
 230 $\pm 0.4 \text{ nA cm}^{-2}$ for the 400 μm diameter device cf. $68.8 \text{ nA cm}^{-2} \pm 2.7 \text{ nA cm}^{-2}$ for the 200 μm diameter device, at
 231 the maximum applied reverse bias (60 V). This suggested that the leakage current did not scale with junction
 232 area. The presence of a non-negligible surface leakage current, possibly due to the devices being unpassivated
 233 [49, 50], cannot be excluded entirely, but the measured leakage currents do not scale with circumference either.
 234 A similar trend was recently reported for GaAs $\text{p}^+\text{-i-n}^+$ mesa X-ray photodiodes of the same size (200 μm and 400
 235 μm diameter) and with the same absorption layer thickness (10 μm) [27]. For the present devices, the difference
 236 in leakage current density with junction area was possibly attributable to damage caused by wirebonding to the
 237 thin metal contacts, resulting in a dominating additional leakage current component.
 238



239

240

Fig. 7. Apparent leakage current density for the 200 μm (circles) and 400 μm (triangles) diameter devices as a function of applied reverse bias, at 20 $^{\circ}\text{C}$.

241

242

243

244

245

246

247

248

249

250

251

The leakage current densities of the presently reported devices were greater than those measured for recently reported GaAs p^+i-n^+ mesa X-ray photodiodes [27]. At an internal electric field strength, E_f , of 50 kV cm^{-1} (corresponding to 51 V applied reverse bias for the GaAs/ $\text{Al}_{0.8}\text{Ga}_{0.2}\text{As}$ devices, assuming E_f was uniform and across only the depleted region), leakage current densities of $61.8 \text{ nA cm}^{-2} \pm 1.5 \text{ nA cm}^{-2}$ and $16.4 \text{ nA cm}^{-2} \pm 0.4 \text{ nA cm}^{-2}$ were measured for the 200 μm diameter and 400 μm diameter devices respectively. At the same E_f , leakage current densities of 15 nA cm^{-2} and 6 nA cm^{-2} were measured for the 200 μm and 400 μm GaAs devices respectively, at 20 $^{\circ}\text{C}$ [27].

252

IV. PHOTON COUNTING X-RAY SPECTROSCOPY

253

A. Experimental measurements and determination of the spectrometers' energy resolutions

254

255

256

257

258

259

260

261

262

263

264

265

266

267

268

269

270

In order to characterise the X-ray detection performance of the GaAs/ $\text{Al}_{0.8}\text{Ga}_{0.2}\text{As}$ SAM APD devices, each detector was connected, in turn, to a custom-made low-noise charge-sensitive feedback-resistorless preamplifier, similar in design to ref. [51]. The preamplifier, in each case, was connected to a shaping amplifier (Ortec 572A) and a multi-channel analyser (Ortec Easy-MCA 8k). An ^{55}Fe X-ray ($\text{Mn K}\alpha = 5.9 \text{ keV}$; $\text{Mn K}\beta = 6.49 \text{ keV}$) source ($\approx 131 \text{ MBq}$) was positioned $\approx 4 \text{ mm}$ above each GaAs/ $\text{Al}_{0.8}\text{Ga}_{0.2}\text{As}$ SAM APD in turn. The resulting spectrometers: S_{200} (using the 200 μm diameter detector) and S_{400} (using the 400 μm diameter detector) were installed within a TAS Micro MT environmental chamber for temperature control. The environmental chamber temperature was set to 20 $^{\circ}\text{C}$, and allowed to stabilise for 1 hour before measurements were taken. A thermocouple was positioned close to the spectrometer such that temperature equilibrium between the environmental chamber and the spectrometer could be monitored. The environmental chamber was purged continually throughout the measurements with dry N_2 ($< 5\%$ relative humidity) as to reduce any humidity related effects [52].

266

267

268

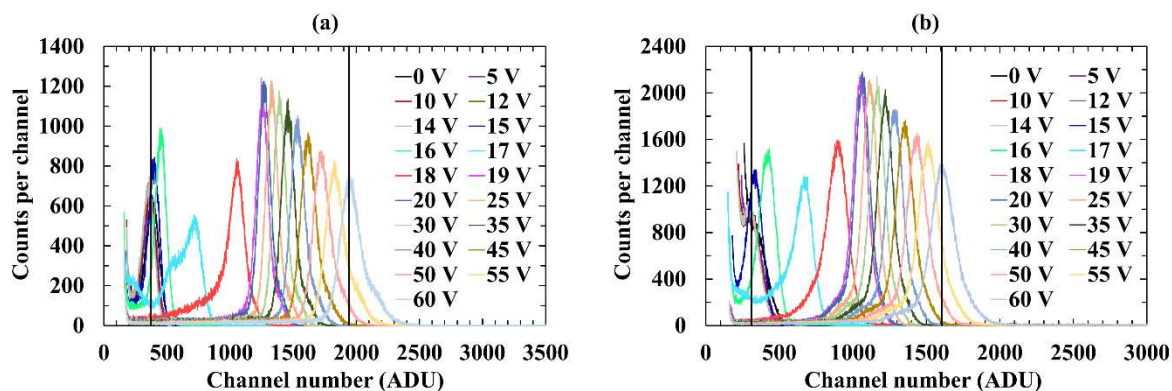
269

270

Spectra were accumulated for each spectrometer as a function of detector applied reverse bias. The applied reverse bias was initially set to 0 V, then increased in 1 V steps up to 50 V. The reverse bias was increased further in steps of 5 V, up to 60 V. After each voltage change, the system was allowed to stabilise for 5 minutes before taking a measurement. Since the two detectors had different active areas, the live time limits of each spectrum were set differently: spectra accumulated with S_{200} had a live time limit of 100 s; spectra accumulated with S_{400}

271 had a live time limit of 25 s. A shaping time of 0.5 μ s was used; this was the best available shaping time for each
 272 system. The accumulated ^{55}Fe spectra for the 200 μ m and 400 μ m diameter GaAs/ $\text{Al}_{0.8}\text{Ga}_{0.2}\text{As}$ SAM APD
 273 spectrometers can be seen in Fig. 8.

274



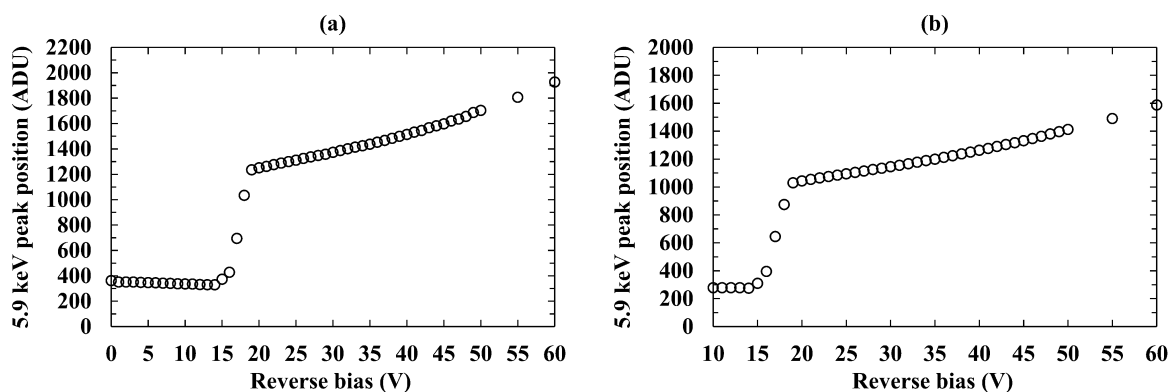
275

276 Fig. 8. Accumulated ^{55}Fe spectra using the spectrometers (a) S₂₀₀ and (b) S₄₀₀. The same shaping time (0.5 μ s) and temperature
 277 (20 °C) were used for all spectra. The vertical black lines indicate the positions of the combined 5.9 keV (Mn K α) and 6.49 keV
 278 (Mn K β) X-ray photopeaks from the ^{55}Fe X-ray source accumulated with the detectors reverse biased at 0 V and 60 V.

279

280 For each accumulated spectrum from the ^{55}Fe X-ray (Mn K α = 5.9 keV; Mn K β = 6.49 keV) source, Gaussian
 281 fitting was applied. The relative emission ratio [53] and the relative detection efficiency of the GaAs/ $\text{Al}_{0.8}\text{Ga}_{0.2}\text{As}$
 282 SAM APDs at these energies were taken into account in fitting the Mn K α and K β peaks. The Mn K α and
 283 K β peaks were not individually resolved by the spectrometer; as such, the peak detected is the combination of the
 284 Mn K α and K β lines. The form of spectroscopic response was consistent with a SAM APD; this was further
 285 exemplified by plotting the change in 5.9 keV peak centroid position (corrected for changes in zero energy noise
 286 peak position and plotted in terms of the MCA's analogue to digital units, ADU, scale) as a function of applied
 287 detector reverse bias, as shown in Fig. 9.

288



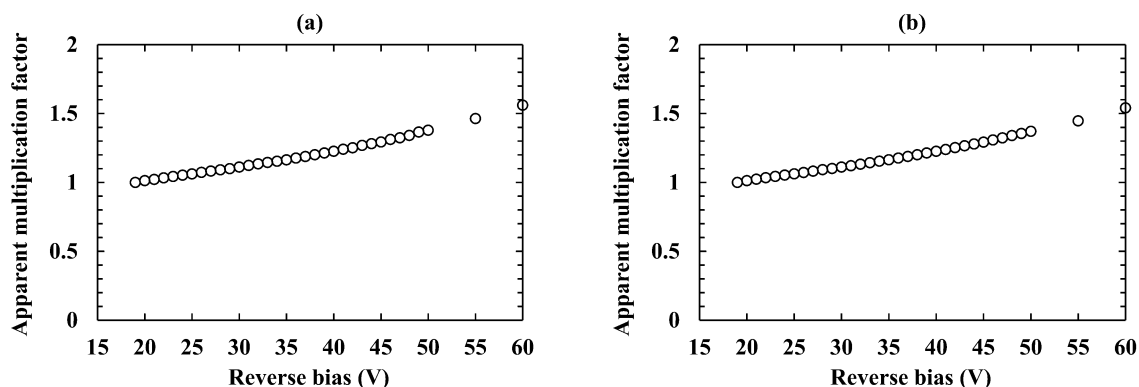
289

290 Fig. 9. Difference, in ADU, between the 0 keV position and the position of the centroid of the fitted 5.9 keV peak as a function
 291 of applied detector reverse bias, at a shaping time of 0.5 μ s, and a temperature of 20 °C for the spectrometers (a) S₂₀₀ and (b)
 292 S₄₀₀.

293

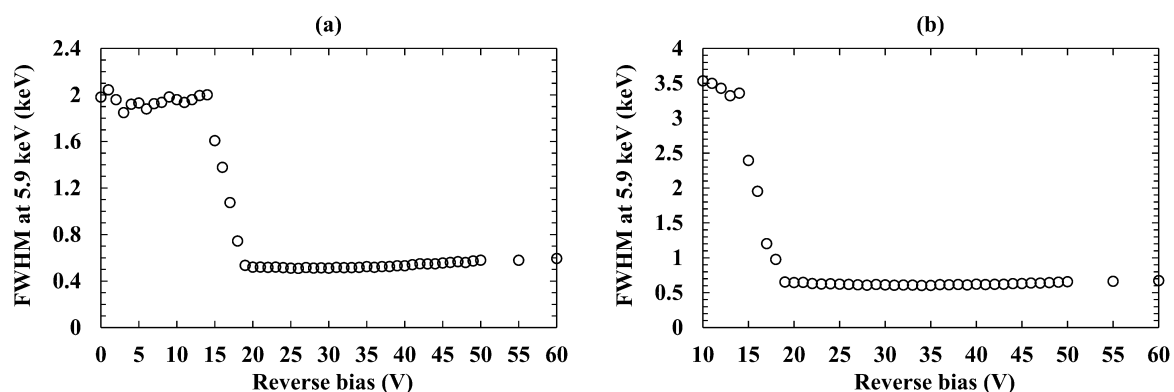
294 The sharp increase in 5.9 keV peak position between 14 V and 19 V for both the 200 μ m and 400 μ m diameter
 295 devices, as shown in Fig. 9, was attributed to an improved charge collection efficiency from reaching the

296 punch-through voltage (see Fig. 2). At applied detector reverse biases less than the punch-through voltage, charge
 297 carriers cannot readily travel through the $\text{Al}_{0.8}\text{Ga}_{0.2}\text{As}$ junction (see Table 1) [18], limiting the charge collection
 298 efficiency. The increasing 5.9 keV peak position as a function of applied detector bias beyond 19 V was a result
 299 of increases in avalanche multiplication. The apparent multiplication factor, M , was calculated for both
 300 spectrometers by calculating the ratio between the fitted 5.9 keV peak position at each bias and the fitted 5.9 keV
 301 peak position at unity gain ($M = 1$) and complete charge collection, assumed to be achieved at $V_R = 19$ V applied
 302 to the detector. The apparent multiplication factor as a function of applied detector reverse bias can be seen in
 303 Fig. 10.
 304



305
 306 Fig. 10. Apparent multiplication factor of the 5.9 keV ^{55}Fe photopeak as a function of applied detector reverse bias for the
 307 spectrometers (a) S₂₀₀ and (b) S₄₀₀, at 20 °C. Unity gain was set to 19 V.

308
 309 The spectra were energy calibrated by assuming a linear variation of output charge with energy and using the
 310 positions of the so called zero energy noise peak and fitted 5.9 keV peak. The energy resolution (FWHM at
 311 5.9 keV) was then calculated for each accumulated spectrum. Fig. 11 presents the energy resolution of each
 312 spectrometer as a function of applied detector reverse bias.
 313



314
 315 Fig. 11. FWHM at 5.9 keV for the spectrometers (a) S₂₀₀ and (b) S₄₀₀ as a function of applied detector reverse bias at a shaping
 316 time of 0.5 μs , and at 20 °C.

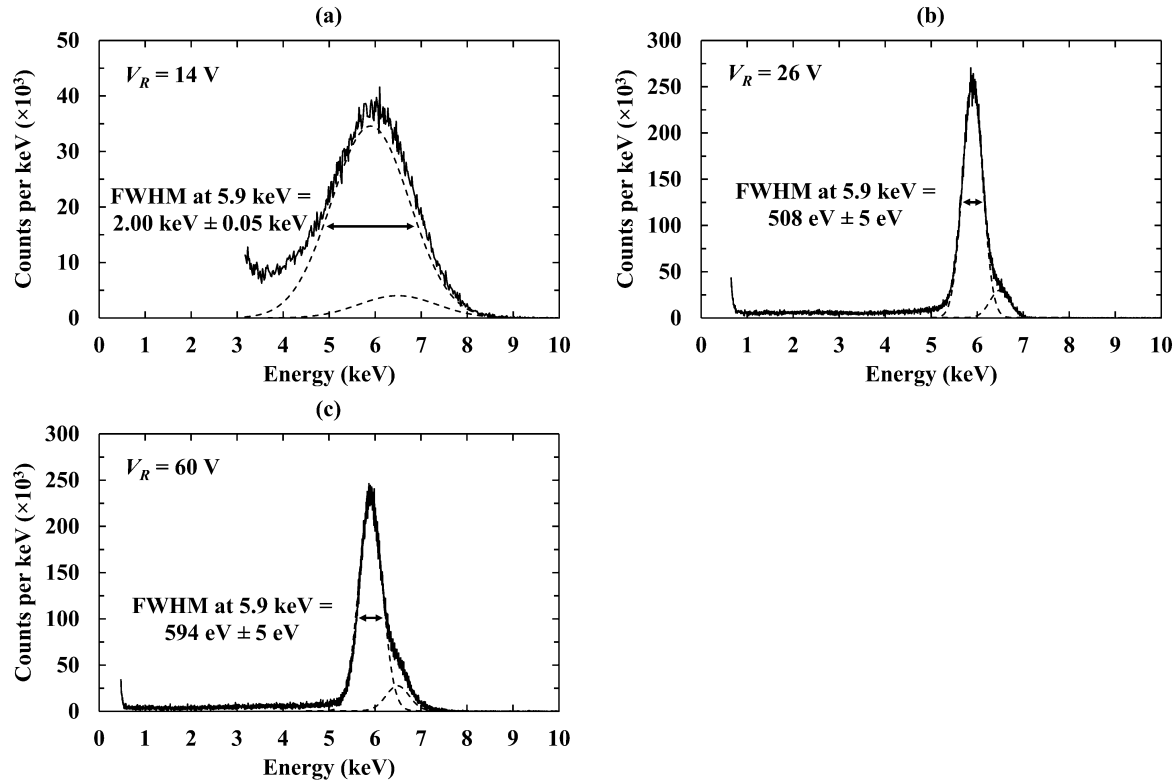
317
 318 The improved charge collection efficiency, due to overcoming the punch-through voltage of the detectors, resulted
 319 in an abrupt improvement in energy resolution (FWHM at 5.9 keV) of the spectroscopic systems around the punch
 320 through voltage, as shown in Fig. 11. At $V_R = 14$ V, the FWHM at 5.9 keV was $2.00 \text{ keV} \pm 0.05 \text{ keV}$ and 3.36 keV

321 ± 0.05 keV for the spectrometers S_{200} and S_{400} , respectively. At $V_R = 19$ V, the FWHM at 5.9 keV was 534 eV
 322 ± 5 eV and 653 eV ± 6 eV for S_{200} and S_{400} , respectively. The best measured energy resolution for the spectrometer
 323 S_{200} was 508 eV ± 5 eV, achieved at $V_R = 26$ V, corresponding to an apparent multiplication factor of 1.1. The
 324 best measured energy resolution for the spectrometer S_{400} was 603 eV ± 6 eV, achieved at $V_R = 34$ V,
 325 corresponding to an apparent multiplication factor of 1.2. ^{55}Fe X-ray spectra accumulated with the spectrometers
 326 S_{200} and S_{400} can be seen in Fig. 12 and Fig. 13 respectively.

327

328 Both the 200 μm diameter and 400 μm diameter GaAs/ $\text{Al}_{0.8}\text{Ga}_{0.2}\text{As}$ SAM APD devices reported here, had
 329 improved performance relative to the recently studied GaAs $\text{p}^+\text{-i-n}^+$ photodiodes [27]. At 20 $^\circ\text{C}$, energy resolutions
 330 of 690 eV and 730 eV FWHM at 5.9 keV were reported for the 200 μm and 400 μm GaAs $\text{p}^+\text{-i-n}^+$ photodiode,
 331 respectively [27]. The presently reported spectrometers also had improved performance compared to the
 332 previously reported GaAs/ $\text{Al}_{0.8}\text{Ga}_{0.2}\text{As}$ SAM APD spectrometers which had a FWHM at 5.9 keV = 1.08 keV at
 333 an avalanche gain of $M = 3.5$ at room temperature [44].

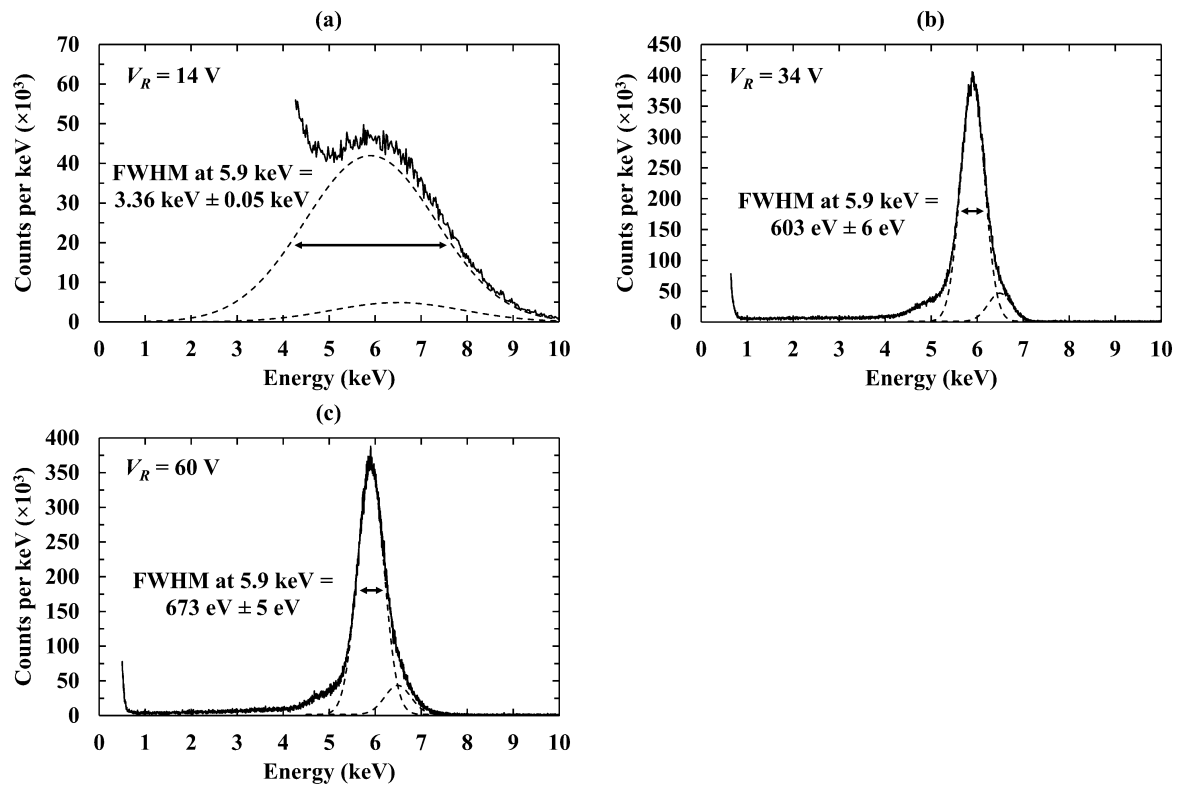
334



335

336 Fig. 12. ^{55}Fe X-ray spectra accumulated with the 200 μm diameter detector based spectrometer, at 20 $^\circ\text{C}$, a shaping time of
 337 0.5 μs , and a reverse bias of (a) 14 V, (b) 26 V, and (c) 60 V. The fitted 5.9 keV (Mn $\text{K}\alpha$) and 6.49 keV (Mn $\text{K}\beta$) peaks have
 338 been plotted (dashed lines). The accumulated spectra have been normalised into counts per keV in order to account for the
 339 differing channel widths.

340



341

342

343

344

345

346

347

348

349

350

351

352

353

354

355

356

357

358

359

360

361

362

363

364

Fig. 13. ^{55}Fe X-ray spectra accumulated with the 400 μm diameter detector based spectrometer, at 20 $^{\circ}\text{C}$, a shaping time of 0.5 μs , and a reverse bias of (a) 14 V, (b) 34 V, (c) and 60 V. The fitted 5.9 keV (Mn $K\alpha$) and 6.49 keV (Mn $K\beta$) peaks have been plotted (dashed lines). The accumulated spectra have been normalised into counts per keV in order to account for the differing channel widths.

B. Origin of the secondary peak in the obtained X-ray spectra

As could be seen in Fig. 13, at sufficiently high applied detector biases ($V_R \geq 17$ V), a small secondary peak appears to the left (low energy) side of the fitted peaks. The secondary peak appears as a shoulder on the main combined peak as they are not resolved from each other. This secondary peak arises as a consequence of the GaAs layer not having a 100 % absorption efficiency for the X-ray photons (see Fig. 4b); some photons are transmitted through the GaAs layer and absorbed in the $\text{Al}_{0.8}\text{Ga}_{0.2}\text{As}$ layers. This can be proven by consideration of the electron-hole pair creation energies of each material.

Due to the difference in electron-hole pair creation energy of GaAs ($\omega_{\text{GaAs}} = 4.19$ eV \pm 0.03 eV at 20 $^{\circ}\text{C}$ [54]) and $\text{Al}_{0.8}\text{Ga}_{0.2}\text{As}$ ($\omega_{\text{AlGaAs}} = 5.07$ eV \pm 0.08 eV at 20 $^{\circ}\text{C}$ [55]), the average number of charge carriers generated in each material by the absorption of a photon of energy, E, also differs.

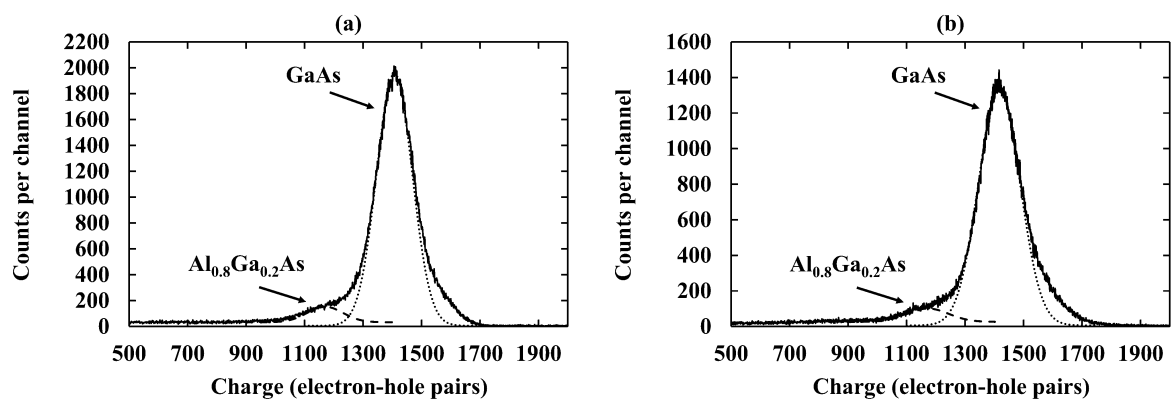
The ratio of the average numbers of charge carriers (N_{AlGaAs} for $\text{Al}_{0.8}\text{Ga}_{0.2}\text{As}$ and N_{GaAs} for GaAs) created by the absorption of a photon of energy, E, in conjunction with the known electron-hole pair creation energy of GaAs, can be used to determine ω_{AlGaAs} , where

$$\omega_{\text{AlGaAs}} = \omega_{\text{GaAs}} \left(\frac{N_{\text{GaAs}}}{N_{\text{AlGaAs}}} \right). \quad (4)$$

365 The primary and secondary peak of the spectra obtained with S_{400} , with the detector biased at 34 V and 60 V
 366 respectively, were fitted with Gaussians for the ^{55}Fe 5.9 keV (Mn $K\alpha$) and 6.49 keV (Mn $K\beta$) peak emissions in
 367 the accepted ratio [53], see Fig. 14; the relative detection efficiencies of the Mn $K\alpha$ and Mn $K\beta$ photons were also
 368 taken into account [49]. The accepted value of ω_{GaAs} was then used in conjunction with Eq. 4 to calculate ω_{AlGaAs} .
 369 With the detector biased at 34 V and 60 V, ω_{AlGaAs} was found to be $5.04 \text{ eV} \pm 0.08 \text{ eV}$ and $5.06 \text{ eV} \pm 0.08 \text{ eV}$
 370 respectively, which are in agreement with the accepted value ($\omega_{\text{AlGaAs}} = 5.07 \text{ eV} \pm 0.08 \text{ eV}$ at 20°C [55]). Thus,
 371 it was demonstrated that the secondary, left shoulder, peak arises as a consequence of X-ray absorption in the
 372 $\text{Al}_{0.8}\text{Ga}_{0.2}\text{As}$ layers by computation of the electron-hole pair creation energy of $\text{Al}_{0.8}\text{Ga}_{0.2}\text{As}$ from the spectra.

373
 374 The secondary peak, clearly visible as a shoulder in Fig. 13 and Fig. 14 (400 μm diameter detector), was less
 375 visible in Fig. 12 (200 μm diameter detector). This was attributed to the size difference between the two
 376 investigated detectors, where the front face of the 400 μm diameter detector received four times more photons
 377 than the 200 μm diameter detector.

378



379

380 Fig. 14. ^{55}Fe X-ray spectra accumulated with S_{400} at a reverse bias of (a) 34 V, and (b) 60 V. Charge calibration was achieved
 381 using the positions of the zero energy noise peak of the preamplifier and the GaAs peak, together with the accepted ω_{GaAs}
 382 value. The dashed and dotted lines are the fitted 5.9 keV (Mn $K\alpha$) peaks for the $\text{Al}_{0.8}\text{Ga}_{0.2}\text{As}$ and GaAs materials respectively;
 383 the 6.49 keV Mn $K\beta$ peaks were considered and included in the analysis but are not shown in the figures for clarity

384

385 C. Noise analysis

386 Four sources of noise influence the energy resolution of a charge-sensitive preamplifier coupled to a
 387 semiconductor detector operating in avalanche mode, these are: the Fano noise, N_F [56]; incomplete charge
 388 collection noise, R [22]; the electronic noise, A [57]; and the excess noise factor, N_x [44].

389

390 The Fano noise, assuming that X-ray photons incident on the reported detectors are absorbed only within the GaAs
 391 absorption region, can be calculated using the equation

392

$$393 N_F = 2.355\omega_{\text{GaAs}}\sqrt{FE/\omega_{\text{GaAs}}}, \quad (5)$$

394

395 where F (0.12 [58]) is the Fano factor of GaAs and the other symbols have previously been defined. N_F was
 396 calculated to be $13 \text{ e}^- \text{ rms}$ at 5.9 keV (128 eV FWHM at 5.9 keV) for the GaAs/ $\text{Al}_{0.8}\text{Ga}_{0.2}\text{As}$ SAM APD. Since

397 the calculated Fano noise was less than the reported spectrometers measured energy resolution, other noise
398 contributions were clearly affecting the spectroscopic system.

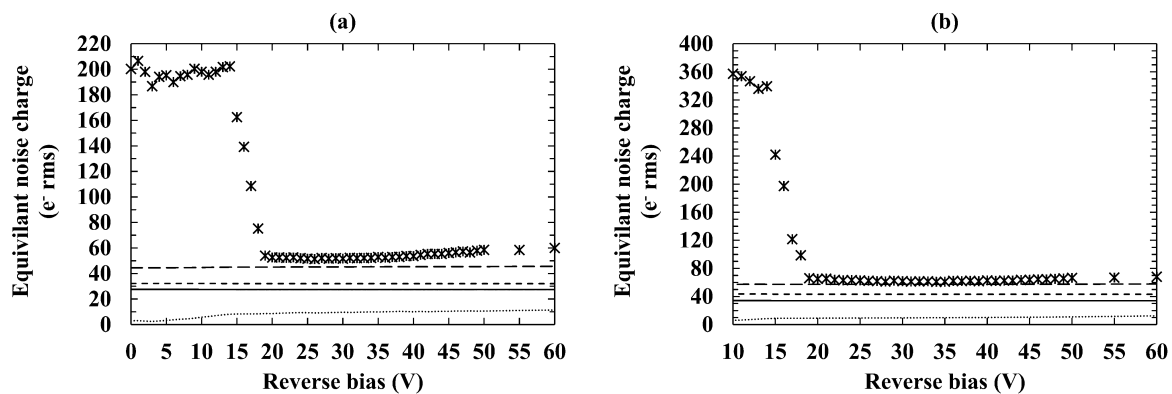
399

400 The electronic noise from the detector and preamplifier of a photodiode X-ray spectrometer consists of dielectric
401 noise, N_D , series white noise (including the induced gate drain current noise), N_{SW} , parallel white noise, N_{PW} , and
402 $1/f$ series noise, $N_{1/f}$ [19]. Dielectric noise is induced by lossy dielectrics close to the input of the spectrometer
403 (e.g. the packaging of the preamplifier input Junction Field-Effect Transistor (JFET) and detector) [59]. Series
404 white noise is caused by capacitances at the input of the spectrometer (e.g. the input JFET (JFET capacitance
405 = 2 pF [60]) and the detector (see Fig. 2)) [27]. Parallel white noise is induced by leakage currents from the input
406 JFET (JFET leakage current = 1 pA [60]) and the detector (see Fig. 6) [27]. For a review of the various noise
407 components, the reader is directed to refs [59, 61, 62].

408

409 The dielectric noise, series white noise, parallel white noise, and $1/f$ series noise contributions were calculated for
410 each spectrometer (S_{200} and S_{400}) via the standard methods for semiconductor X-ray devices connected to
411 charge-sensitive preamplifiers [59]. The results can be seen in Fig. 15. It should be noted that, in the case of the
412 dielectric noise contributions, only a lower bound value could be calculated directly; whilst dielectric noise from
413 the JFET, feedback capacitor, and GaAs/ $Al_{0.8}Ga_{0.2}As$ SAM APD device could be estimated [19, 25], additional
414 lossy dielectrics close to the preamplifier input could have also contributed to the noise. Similarly, due to the
415 prototype nature of the preamplifier, the presence of unknown capacitances may have also added to the series
416 white noise contribution. The dielectric noise and series white noise were thus considered in two parts: known
417 noise contributions and stray noise contributions. Subtracting the expected Fano noise and the electronic noise
418 contributions ($1/f$ noise, parallel white noise, known series white noise (including induced gate drain current
419 noise), and known dielectric noise) from the measured FWHM in quadrature, yields a combination of stray series
420 white noise, stray dielectric noise, incomplete charge collection noise, excess noise, and possibly stray parallel
421 white noise contributions (so called the remaining noise contribution). Changes in detector capacitance were
422 included in the known series white noise and known dielectric noise calculations, whilst the JFET was considered
423 to contribute a constant capacitance (2 pF [60]) to both calculations. A constant JFET leakage current (1 pA [60])
424 was included in the known parallel white noise calculation.

425



426

427 Fig. 15. Calculated noise contributions of the spectrometers (a) S_{200} and (b) S_{400} as a function of applied detector reverse bias
428 at a shaping time of $0.5 \mu s$, and at $20^\circ C$: total noise (stars); sum of the calculated noise contributions (long dashed line); known
429 series white noise (short dashed line); known dielectric noise (solid line); calculated parallel white noise (dotted line).

430

431

432

433

434

435

436

437

438

439

440

441

442

443

444

445

446

447

448

449

450

451

452

453

454

455

456

457

458

459

460

461

462

463

464

465

466

467

468

As per Fig. 15, the total sum of the calculated noise contributions (Fano noise, $1/f$ noise, known series white noise, known dielectric noise, and parallel white noise, added in quadrature) did not account for the measured total noise (FWHM at 5.9 keV) of the 200 μm and 400 μm diameter detector based spectroscopic systems. At an applied detector reverse bias of 10 V, the total noise of each system was $198\text{ e}^- \text{ rms} \pm 5\text{ e}^- \text{ rms}$, and $357\text{ e}^- \text{ rms} \pm 5\text{ e}^- \text{ rms}$ for S_{200} and S_{400} , respectively. At the same applied bias (10 V), the total sum of the calculated noise contributions was $44.7\text{ e}^- \text{ rms} \pm 0.4\text{ e}^- \text{ rms}$ and $57.4\text{ e}^- \text{ rms} \pm 0.2\text{ e}^- \text{ rms}$, respectively. This discrepancy was attributed in part to incomplete charge collection noise, where charge carriers cannot readily travel through the $\text{Al}_{0.8}\text{Ga}_{0.2}\text{As}$ junction before the punch-through voltage [18] (see Section IV.A). Stray dielectric noise, stray series white noise, and any stray parallel white noise contributions, arising from the spectroscopic systems, would have also contributed to the measured total noise.

As the applied detector reverse bias was further increased ($14\text{ V} < V_R < 19\text{ V}$), the measured total noise (FWHM at 5.9 keV) of each spectrometer improved (reduced). At 19 V applied detector reverse bias, the total noise was $54.0\text{ e}^- \text{ rms} \pm 0.5\text{ e}^- \text{ rms}$ and $66.0\text{ e}^- \text{ rms} \pm 0.6\text{ e}^- \text{ rms}$ for the spectrometers S_{200} and S_{400} , respectively. The total sum of the calculated noise contributions, at the same applied detector reverse bias (19 V), was $45.0\text{ e}^- \text{ rms} \pm 0.4\text{ e}^- \text{ rms}$ and $57.3\text{ e}^- \text{ rms} \pm 0.2\text{ e}^- \text{ rms}$ for the spectrometers S_{200} and S_{400} , respectively. This, in part, indicated that incomplete charge collection noise reduced as the punch-through voltage ($\approx 14\text{ V}$) was exceeded.

At the optimal applied detector reverse bias for each spectrometer (26 V and 34 V for the spectrometers S_{200} and S_{400} respectively), the measured apparent noise was $51.4\text{ e}^- \text{ rms} \pm 0.5\text{ e}^- \text{ rms}$ and $61.0\text{ e}^- \text{ rms} \pm 0.6\text{ e}^- \text{ rms}$ for the spectrometers S_{200} and S_{400} , respectively. The total sum of the calculated noise contributions, at the same optimal applied detector reverse bias (26 V and 34 V for S_{200} and S_{400} respectively), was $45.1\text{ e}^- \text{ rms} \pm 0.4\text{ e}^- \text{ rms}$ and $57.4\text{ e}^- \text{ rms} \pm 0.2\text{ e}^- \text{ rms}$ for the spectrometers S_{200} and S_{400} , respectively. The apparent decrease in remaining noise contribution between 19 V and the optimal applied detector reverse bias of each spectrometer indicated a net benefit due to avalanche multiplication.

At the maximum applied detector reverse bias (60 V) an apparent noise of $60.1\text{ e}^- \text{ rms} \pm 0.5\text{ e}^- \text{ rms}$ and $68.0\text{ e}^- \text{ rms} \pm 0.5\text{ e}^- \text{ rms}$ was measured for S_{200} and S_{400} , respectively. The total sum of the calculated noise contributions at the same applied detector reverse bias (60 V), was $45.6\text{ e}^- \text{ rms} \pm 0.4\text{ e}^- \text{ rms}$ and $57.9\text{ e}^- \text{ rms} \pm 0.2\text{ e}^- \text{ rms}$, respectively. The increased discrepancy between the measured apparent noise (FWHM at 5.9 keV) and the total sum of the calculated noise contributions may have arisen from a larger than expected parallel white noise at high biases or from increasing excess noise due to avalanche multiplication.

D. Improvements in energy resolution due to avalanche multiplication

In order to determine whether avalanche multiplication affected the energy resolution of the reported spectrometers, the measured energy resolution (FWHM at 5.9 keV) was compared to the expected non-avalanche energy resolution of each spectrometer.

469 The expected non-avalanche energy resolution was calculated by assuming incomplete charge collection noise
 470 became negligible at $V_R \geq 19$ V, avalanche multiplication was not present at $V_R \leq 19$ V, and any stray noises
 471 contributing to the remaining noise contribution (see Section IV.C) were independent of applied reverse bias.
 472 Given these assumptions, the remaining noise contribution at $V_R = 19$ V for both spectrometers represents the
 473 non-avalanche mode remaining noise contribution across the applied reverse bias range ($19 \text{ V} \leq V_R \leq 60 \text{ V}$). The
 474 remaining noise contribution at $V_R = 19$ V was calculated to be $29.8 e^- \text{ rms} \pm 1.1 e^- \text{ rms}$ and $32.8 e^- \text{ rms} \pm 1.6 e^- \text{ rms}$
 475 for S_{200} and S_{400} , respectively.

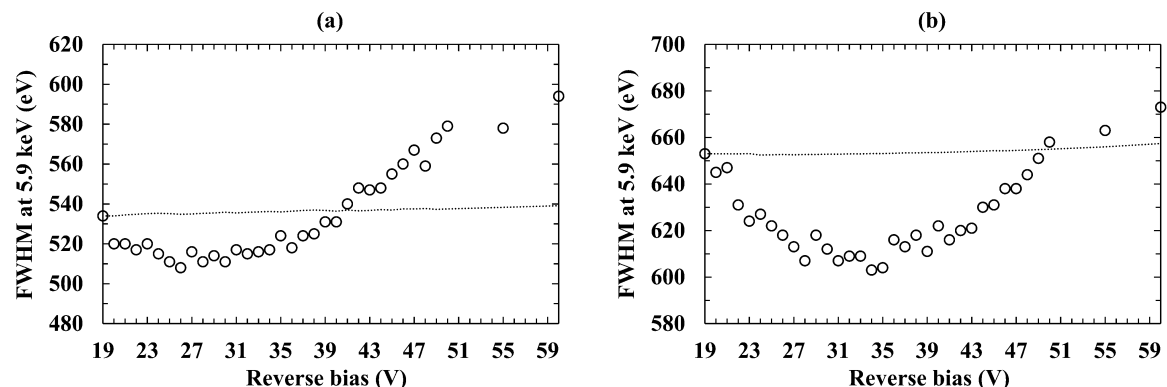
476

477 Adding in quadrature the remaining noise contribution at $V_R = 19$ V to the calculated known noise contributions
 478 at each investigated applied detector reverse bias yields the expected non-avalanche energy resolution as a
 479 function of applied reverse bias within the range $19 \text{ V} \leq V_R \leq 60 \text{ V}$. The expected non-avalanche energy resolution,
 480 and measured avalanche energy resolution, at each applied reverse bias for the spectrometers S_{200} and S_{400} , can be
 481 seen in Fig. 16.

482

483 At an applied detector reverse bias of 26 V ($M = 1.1$), an expected non-avalanche energy resolution of 535 eV
 484 $\pm 7 \text{ eV}$ FWHM at 5.9 keV was calculated for the spectrometer S_{200} . Given the same spectrometer and the same
 485 applied detector reverse bias (26 V), an energy resolution of $508 \text{ eV} \pm 5 \text{ eV}$ was measured. As for the spectrometer
 486 S_{400} , at an applied detector reverse bias of 34 V ($M = 1.2$), an expected non-avalanche energy resolution of 653 eV
 487 $\pm 8 \text{ eV}$ FWHM at 5.9 keV was calculated. At the same applied detector reverse bias (34 V), an energy resolution
 488 of $603 \text{ eV} \pm 6 \text{ eV}$ was measured. As such, it can be concluded that a noticeable benefit from small avalanche
 489 multiplication gains ($M \leq 1.4$) was measured. This conclusion is further supported by recent results from non-
 490 avalanche GaAs p^+i-n^+ photodiodes. Those photodiodes were of identical design to the devices reported here
 491 except that they did not have the AlGaAs avalanche layer [27]. At 20°C , energy resolutions of 690 eV and 730 eV
 492 FWHM at 5.9 keV were reported for the 200 μm and 400 μm GaAs p^+i-n^+ photodiode, respectively [27]. Thus
 493 it has been demonstrated that the addition of an avalanche layer can lead to improvement of the energy resolution
 494 in X-ray photodiodes.

495



496

497 Fig. 16. Expected non-avalanche FWHM at 5.9 keV, assuming no incomplete charge collection noise at $V_R \geq 19$ V (dotted
 498 line), as a function of applied detector reverse bias to the spectrometers (a) S_{200} and (b) S_{400} . The measured FWHM at 5.9 keV
 499 (circles) has been included.

500

501

V. CONCLUSION

502 A 200 μm diameter and a 400 μm diameter, custom-made, circular GaAs/ $\text{Al}_{0.8}\text{Ga}_{0.2}\text{As}$ separate absorption and
503 multiplication (SAM) X-ray photodiode have each been characterised at room temperature (20 $^{\circ}\text{C}$), and
504 investigated for their response to ^{55}Fe X-rays (Mn $K\alpha = 5.9$ keV; Mn $K\beta = 6.49$ keV) source. Each device
505 consisted of a 10 μm thick GaAs absorption layer and a 0.1 μm thick $\text{Al}_{0.8}\text{Ga}_{0.2}\text{As}$ multiplication layer.

506

507 Capacitance measurements indicated a punch-through voltage of ≈ 14 V for both devices. A capacitance of
508 1.12 pF and 2.20 pF (each ± 0.4 fF) was measured for the 200 μm and 400 μm diameter devices respectively at
509 the maximum applied reverse bias (60 V). The capacitance measurements indicated that both devices were fully
510 depleted at $V_R \geq 50$ V, reporting a depletion width consistent with growth specifications (see Table 1).

511

512 The best measured energy resolution achieved at 20 $^{\circ}\text{C}$ for the spectrometer S_{200} was 508 eV ± 5 eV FWHM at
513 5.9 keV, at an applied detector reverse bias of 26 V, corresponding to an apparent multiplication factor of 1.1.

514 The best measured energy resolution at 20 $^{\circ}\text{C}$ for the spectrometer S_{400} was 603 eV ± 6 eV FWHM at 5.9 keV, at
515 an applied detector reverse bias of 34 V, corresponding to an apparent multiplication factor of 1.2. Further
516 increasing the applied detector reverse bias increased (worsened) the energy resolution (e.g. 594 eV ± 5 eV
517 FWHM at 5.9 keV and 673 eV ± 5 eV FWHM at 5.9 keV for the spectrometers S_{200} and S_{400} respectively, at an
518 applied detector reverse bias of 60 V). This indicated that any benefits from further increasing avalanche gain
519 were exceeded by increases in excess noise and/or parallel white noise.

520

521 In order to determine whether avalanche multiplication affected the energy resolution of the spectrometers, the
522 measured energy resolution (FWHM at 5.9 keV) was compared to the expected non-avalanche energy resolution
523 of each spectrometer (see Section IV.D). The results indicated a noticeable benefit from small avalanche
524 multiplication gains ($M \leq 1.4$). At an applied detector reverse bias of 26 V ($M = 1.1$), an expected non-avalanche
525 energy resolution of 535 eV FWHM at 5.9 keV was calculated for the spectrometer S_{200} . Given the same
526 spectrometer and the same applied detector reverse bias (26 V), an energy resolution of 508 eV FWHM at 5.9 keV
527 was measured. Similarly, at an applied detector reverse bias of 34 V ($M = 1.2$), an expected non-avalanche energy
528 resolution of 653 eV FWHM at 5.9 keV was calculated for the spectrometer S_{400} . Given the same spectrometer
529 and the same applied detector reverse bias (34 V), an energy resolution of 603 eV FWHM at 5.9 keV was
530 measured. The results were supported further (and set in context) by a recent study using non-avalanche GaAs
531 $\text{p}^+\text{-i-n}^+$ photodiodes which did not have an AlGaAs avalanche layer [27]. At 20 $^{\circ}\text{C}$, energy resolutions of 690 eV
532 and 730 eV FWHM at 5.9 keV were reported for the 200 μm and 400 μm GaAs $\text{p}^+\text{-i-n}^+$ photodiodes, respectively
533 [27]. The results indicated that introducing a separate AlGaAs multiplication layer can be beneficial to GaAs
534 photodiodes.

535

536 The energy resolution (FWHM at 5.9 keV) reported here is the best so far reported for GaAs/ $\text{Al}_x\text{Ga}_{1-x}\text{As}$ SAM
537 APD X-ray spectrometers at room temperature. Energy resolutions of 1.08 keV FWHM at 5.9 keV [44] and
538 900 eV FWHM at 13.96 keV have been reported previously [18]. The measured energy resolution was also better
539 than recently investigated non-avalanche $\text{Al}_x\text{Ga}_{1-x}\text{As}$ detector based X-ray spectrometers, where an energy
540 resolution of 760 eV FWHM at 5.9 keV was reported at room temperature [26]. However, the energy resolutions
541 reported here are modest when compared to the best reported results for the best non-avalanche GaAs based X-ray

542 spectrometers (266 eV [3] and 300 eV [28] FWHM at 5.9 keV at room temperature) and the best Si based X-ray
543 spectrometers (141 eV FWHM at 5.9 keV by [63] and 134 eV FWHM at 5.9 keV [64]), when those detectors are
544 coupled to ultra-low-noise electronics better than those used for the investigations reported in the present article.

545

546 Despite the achieved energy resolutions of the presently reported GaAs/Al_xGa_{1-x}As SAM APDs being not yet as
547 good when compared to other more developed materials, X-ray spectrometers with modest energy resolutions can
548 still provide important scientific contributions. For example, D-CIXS aboard SMART-1 [65] had an energy
549 resolution of 420 eV FWHM at 4.5 keV [66] and measured, for the first time, Ti K α (4.51 keV) X-ray fluorescence
550 on the lunar surface [66]. An X-ray spectrometer with similar or slightly improved energy resolution, that is also
551 radiation hard and temperature tolerant, could therefore find utility in future space science missions to harsh
552 environments.

553

554 In future, the temperature dependence of the devices' electrical characteristics and X-ray detection performance
555 will be studied. New SAM APDs will be fabricated in array format and characterised. Devices with thicker
556 absorption regions will be grown to improve the quantum efficiency (thereby also reducing/eliminating the
557 observed secondary photopeak as discussed in Section IV.B), and staircase avalanche regions implemented. A
558 thicker absorption region would also reduce the detector capacitance, reducing the series white noise, and
559 potentially improving the energy resolution of the spectrometer.

560

561 **AUTHORS' DATA STATEMENT**

562 The data that supports the findings of this study are available within the article [and its supplementary material].

563

564 **ACKNOWLEDGEMENTS**

565 This work was supported in part by Science and Technology Facilities Council, UK, Grants ST/P001815/1 and
566 ST/M004635/1. M.D.C.W. acknowledges funding received from University of Sussex, UK, in the form of a PhD
567 scholarship. A.M.B. acknowledges funding from the Leverhulme Trust, UK, in the form of a 2016 Philip
568 Leverhulme Prize.

569

570 ¹P. Majewski, L. Andricek, A. Bahr, G. De Vita, B. Gunther, K. Hermenau, M. Hilchenbach, T. Lauf, P. Lechner,
571 G. Lutz, D. Miessner, M. Porro, J. Reiffers, R. Richter, G. Schaller, M. Schnecke, F. Schopper, H. Soltau, A.
572 Stefanescu, R. Strecker, L. Struder, and J. Treis, 2012, IEEE Transactions on Nuclear Science 59, 2479 (2012).

573

574 ²D.N. Burrows, J.E. Hill, J.A. Nousek, J.A. Kennea, A. Wells, J.P. Osborne, A.F. Abbey, A. Beardmore, K.
575 Mukerjee, A.D.T. Short, G. Chincarini, S. Campana, O. Citterio, A. Moretti, C. Pagani, G. Tagliaferri, P. Giommi,
576 M. Capalbi, F. Tamburelli, L. Angelini, G. Cusumano, H.W. Bräuninger, W. Burkert, and G.G. Hartner, Space
577 Science Reviews 120, 165 (2005).

578

579 ³A. Owens, M. Bavdaz, A. Peacock, A. Poelaert, H. Andersson, S. Nenonen, H. Sipila, L. Tröger, and G.
580 Bertuccio, Journal of Applied Physics 90, 5376 (2001).

581

- 582 ⁴G. Bertuccio, R. Casiraghi, D. Maiocchi, A. Owens, M. Bavdaz, A. Peacock, H. Andersson, and S. Nenonen,
583 IEEE Transactions on Nuclear Science 50, 723 (2003).
584
- 585 ⁵A.M. Barnett, J.E. Lees, D.J. Bassford, J.S. Ng, C.H. Tan, N. Babazadeh, and R.B. Gomes, Nuclear Instruments
586 and Methods in Physics Research Section A 654, 336 (2011).
587
- 588 ⁶G. Lioliou, X. Meng, J.S. Ng, and A.M. Barnett, Journal of Applied Physics 119, 124507 (2016).
589
- 590 ⁷A. Owens, M. Bavdaz, A. Peacock, A. Poelaert, H. Andersson, S. Nenonen, L. Tröger, and G. Bertuccio, Nuclear
591 Instruments and Methods in Physics Research Section A 466, 168 (2001).
592
- 593 ⁸H. Kagan, Nuclear Instruments and Methods in Physics Research Section A 546, 222 (2005).
594
- 595 ⁹M. Zhang, B. Gu, L. Wang, and Y. Xia, Physics Letters A 332, 320 (2004).
596
- 597 ¹⁰G. Bertuccio, and R. Casiraghi, IEEE Transactions on Nuclear Science 50, 175 (2003).
598
- 599 ¹¹G. Bertuccio, S. Caccia, D. Puglisi, and D. Macera, Nuclear Instruments and Methods in Physics Research
600 Section A 652, 193 (2011).
601
- 602 ¹²S. Zhao, T. Gohil, G. Lioliou, and A.M. Barnett, Nuclear Instruments and Methods in Physics Research Section
603 A 830, 1 (2016).
604
- 605 ¹³S. Butera, G. Lioliou, A.B. Krysa, and A.M. Barnett, Scientific Reports 7, 10206 (2017).
606
- 607 ¹⁴G. Lioliou, A.B. Krysa, and A.M. Barnett, Journal of Applied Physics 124, 195704 (2018).
608
- 609 ¹⁵A. Auckloo, J.S. Cheong, X. Meng, C.H. Tan, J.S. Ng, A.B. Krysa, R.C. Tozer, and J.P.R. David, Journal of
610 Instrumentation 11, P03021 (2016).
611
- 612 ¹⁶S. Butera, G. Lioliou, A.B. Krysa, and A.M. Barnett, Journal of Applied Physics 120, 024502 (2016).
613
- 614 ¹⁷S. Butera, T. Gohil, G. Lioliou, A.B. Krysa, and A.M. Barnett, Journal of Applied Physics 120, 174503 (2016).
615
- 616 ¹⁸J. Lauter, D. Protić, A. Förster, and H. Lüth, Nuclear Instruments and Methods in Physics Research Section A
617 356, 324 (1995).
618
- 619 ¹⁹A.M. Barnett, G. Lioliou, and J.S. Ng, Nuclear Instruments and Methods in Physics Research Section A 774, 29
620 (2015).
621

- 622 ²⁰A. Silenas, J. Pozela, K. Pozela, L. Dapkus, and V. Juciene, Nuclear Instruments and Methods in Physics
623 Research Section A 563, 21 (2006).
624
- 625 ²¹M.D.C. Whitaker, S. Butera, G. Lioliou, and A.M. Barnett, Journal of Applied Physics 122, 034501 (2017).
626
- 627 ²²A. Owens, and A. Peacock, Nuclear Instruments and Methods in Physics Research Section A 531, 18 (2004).
628
- 629 ²³B.L. Henke, E.M. Gullikson, and J.C. Davis, Atomic Data and Nuclear Data Tables 54, 181 (1993).
630
- 631 ²⁴G.P. Summers, E.A. Burke, P. Shapiro, S.R. Messenger, and R.J. Walters, IEEE Transactions on Nuclear
632 Science 40, 1372 (1993).
633
- 634 ²⁵G. Lioliou, and A.M. Barnett, Nuclear Instruments and Methods in Physics Research Section A 801, 63 (2015).
635
- 636 ²⁶M.D.C. Whitaker, G. Lioliou, and A.M. Barnett, Nuclear Instruments and Methods in Physics Research Section
637 A 899, 106 (2018).
638
- 639 ²⁷G. Lioliou, M.D.C. Whitaker, and A.M. Barnett, Journal of Applied Physics 122, 244506 (2017).
640
- 641 ²⁸C. Erd, A. Owens, G. Brammertz, M. Bavdaz, A. Peacock, V. Lämsä, S. Nenonen, H. Andersson, and N. Haack,
642 Nuclear Instruments and Methods in Physics Research Section A 487, 78 (2002).
643
- 644 ²⁹A.M. Barnett, D.J. Bassford, J.E. Lees, J.S. Ng, C.H. Tan, and J.P.R. David, Nuclear Instruments and Methods
645 in Physics Research Section A 621, 453 (2010).
646
- 647 ³⁰J.C. Campbell, Journal of Lightwave Technology 25, 109 (2007).
648
- 649 ³¹J.P.R. David, and C.H. Tan, IEEE Journal of Selected Topics in Quantum Electronics 14, 998 (2008).
650
- 651 ³²J. Kou1, K. Tian, C. Chu, Y. Zhang, X. Zhou, Z. Feng, and Z. Zhang, Nanoscale Research Letters 14, 396
652 (2019).
653
- 654 ³³X. Zhou, X. Tan, Y. Lv, Y. Wang, J. Li, T. Han, H. Guo, S. Liang, Z. Zhang, Z. Feng, and S. Cai, IEEE Electron
655 Device Letters 40, 1591 (2019).
656
- 657 ³⁴S.M. Sze, Physics of Semiconductor Devices, 3rd ed. (John Wiley & Sons, New Jersey, 2007).
658
- 659 ³⁵A.M. Barnett, J.E. Lees, D.J. Bassford, J.S. Ng, C.H. Tan, and R.B. Gomez, Nuclear Instruments and Methods
660 in Physics Research Section A 626, 25 (2011).
661

- 662 ³⁶C.H. Tan, J.P.R. David, S.A. Plimmer, G.J. Rees, R.C. Tozer, and R. Grey, IEEE Transactions on Electron
663 Devices 48, 1310 (2001).
664
- 665 ³⁷R.J. McIntyre, IEEE Transactions on Electron Devices 13, 164 (1966).
666
- 667 ³⁸C.H. Tan, R.B. Gomes, J.P.R. David, A.M. Barnett, D.J. Bassford, J.E. Lees, and J.S. Ng, IEEE Transactions on
668 Electron Devices 58, 1696 (2011).
669
- 670 ³⁹G.W. Fraser, X-ray Detectors in Astronomy (Cambridge University Press, Cambridge, 2016).
671
- 672 ⁴⁰J. David, 2016, Nature Photonics 10, 364 (2016).
673
- 674 ⁴¹F. Capasso, T. Won-Tien, and G.F. Williams, IEEE Transactions on Electron Devices 30, 381 (1983).
675
- 676 ⁴²G. Ripamonti, F. Capasso, A.L. Hutchinson, D.J. Muehlner, J.F. Walker, and R.J. Malik, Nuclear Instruments
677 and Methods in Physics Research Section A 288, 99 (1990).
678
- 679 ⁴³C.K. Chia, B.K. Ng, J.P.R. David, G.J. Rees, R.C. Tozer, M. Hopkinson, R.J. Airey, and P.N. Robson, Journal
680 of Applied Physics 94, 2631 (2003).
681
- 682 ⁴⁴R.B. Gomes, C.H. Tan, X. Meng, J.P.R. David, and J.S. Ng, Journal of Instrumentation 9, P03014 (2014).
683
- 684 ⁴⁵S. Butera, M.D.C. Whitaker, G. Lioliou, and A.M. Barnett, Scientific Reports 6, 38409 (2016).
685
- 686 ⁴⁶M.R. Brozel, and G.E. Stillman, Properties of Gallium Arsenide, 3rd ed. (The Institution of Electrical Engineers,
687 London, 1996).
688
- 689 ⁴⁷S. Adachi, Properties of aluminium gallium arsenide, EMIS Datareviews Series No. 7 INSPEC (The Institution
690 of Electrical Engineers, London, 1993).
691
- 692 ⁴⁸R.A. Stradling, and P.C. Klipstein, Growth and characterisation of semiconductors, 1st ed. (IOP Publishing Ltd,
693 Bristol, 1991).
694
- 695 ⁴⁹G. Lioliou, Wide Bandgap Semiconductor Radiation Detectors for Extreme Environments, PhD Thesis
696 (Department of Engineering and Informatics, University of Sussex, Sussex, 2017).
697
- 698 ⁵⁰M. Takenaka, K. Morii, M. Sugiyama, Y. Nakano, and S. Takagi, Optics Express 20, 8718 (2012).
699
- 700 ⁵¹G. Bertuccio, P. Rehak, and D. Xi, Nuclear Instruments and Methods in Physics Research Section A 326, 71
701 (1993).

702

703 ⁵²A.M. Barnett, J.E. Lees, and D.J. Bassford, *Journal of Instrumentation* 8, 1 (2013).

704

705 ⁵³U. Schötzig, *Applied Radiation and Isotopes* 53, 469 (2000).

706

707 ⁵⁴G. Bertuccio, and D. Maiocchi, *Journal of Applied Physics* 92, 1248 (2002).

708

709 ⁵⁵A.M. Barnett, J.E. Lees, and D.J. Bassford, *Applied Physics Letters* 102, 181119 (2013).

710

711 ⁵⁶G. Bertuccio, *IEEE Solid State Circuits Magazine* 4, 36 (2012).

712

713 ⁵⁷G. Lioliou, and A.M. Barnett, *Nuclear Instruments and Methods in Physics Research Section A* 801, 63 (2015).

714

715 ⁵⁸G. Bertuccio, A. Pullia, J. Lauter, A. Forster, and H. Luth, *IEEE Transactions on Nuclear Science* 44, 1 (1997).

716

717 ⁵⁹G. Bertuccio, A. Pullia, and G. De Geronimo, *Nuclear Instruments and Methods in Physics Research Section A*
718 380, 301 (1996).

719

720 ⁶⁰Siliconix, 2N4416/2N4416A/SST4416 N-Channel JFETs, Data Sheet, 70242 S-04028, Rev. F, 04-Jun-01
721 (Vishay Electronic GmbH, Selb, 2001).

722

723 ⁶¹A.M. Barnett, J.E. Lees, D.J. Bassford, and J.S. Ng, *Nuclear Instruments and Methods in Physics Research*
724 *Section A* 673, 10 (2012).

725

726 ⁶²G. Bertuccio, and A. Pullia, 1993, *Review of Scientific Instruments* 64, 3294 (1993).

727

728 ⁶³G. Bertuccio, M. Ahangarianabhari, C. Graziani, D. Macera, Y. Shi, A. Rachevski, I. Rashevskaya, A. Vacchi,
729 G. Zampa, N. Zampa, P. Bellutti, G. Giacomini, A. Picciotto, and C. Piemonte, 2015, A Silicon Drift
730 Detector-CMOS front-end system for high resolution X-ray spectroscopy up to room temperature, *Journal of*
731 *Instrumentation* 10, P01002 (2015).

732

733 ⁶⁴J. Müller-Seidlitz, R. Andritschke, A. Bähr, N. Meidinger, S. Ott, R.H. Richter, W. Treberspurg, and J. Treis,
734 Spectroscopic performance of DEPFET active pixel sensor prototypes suitable for the high count rate Athena
735 WFI detector (SPIE Astronomical Telescopes + Instrumentation, Edinburgh, 2016).

736

737 ⁶⁵M. Grande, R. Browning, N. Waltham, D. Parker, S.K. Dunkin, B. Kent, B. Kellett, C.H. Perry, B. Swinyard,
738 A. Perry, J. Feraday, C. Howe, G. McBride, K. Phillips, J. Huovelin, P. Muhli, P.J. Hakala, O. Vilhu, J. Laukkanen,
739 N. Thomas, D. Hughes, H. Alleyne, M. Grady, R. Lundin, S. Barabash, D. Baker, P.E. Clark, C.D. Murray, J.
740 Guest, I. Casanova, L.C. D'uston, S. Maurice, B. Foing, D.J. Heather, V. Fernandes, K. Muinonen, S.S. Russell,



This is the author's peer reviewed, accepted manuscript. However, the online version of record will be different from this version once it has been copyedited and typeset.

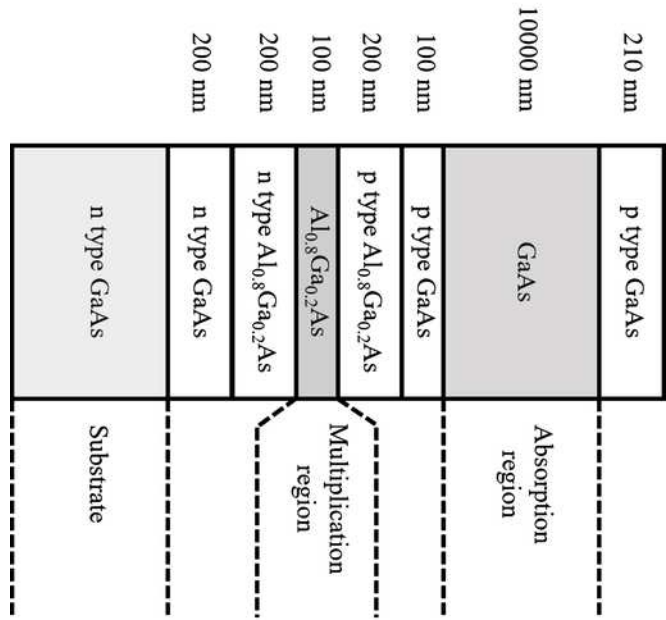
PLEASE CITE THIS ARTICLE AS DOI: 10.1063/5.0009830

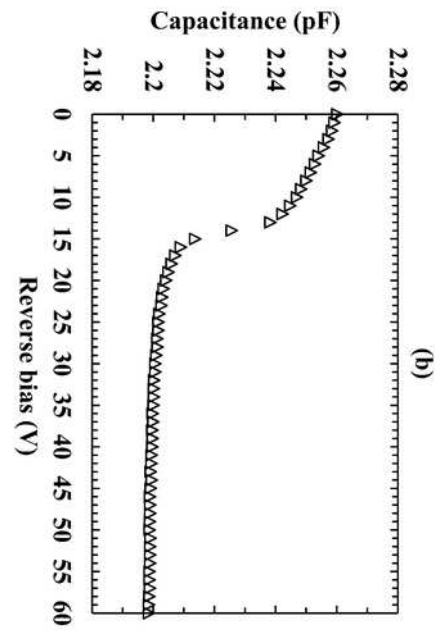
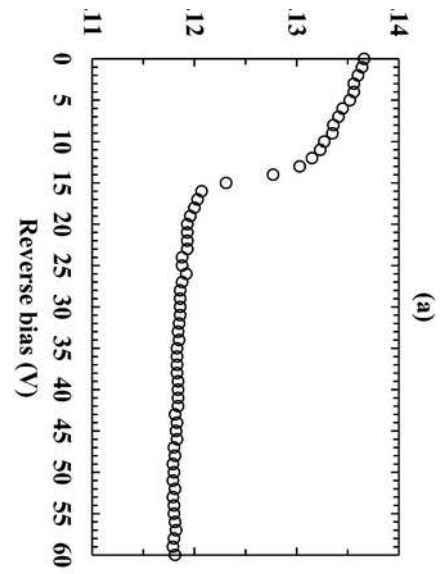
- 741 A. Christou, C. Owen, P. Charles, H. Koskinen, M. Kato, K. Sipilä, S. Nenonen, M. Holmstrom, N. Bhandari, R.
742 Elphic, and D. Lawrence, *Planetary and Space Science* 51, 427 (2003).
743
744 ⁶⁶B.M. Swinyard, K.H. Joy, B.J. Kellett, I.A. Crawford, M. Grande, C.J. Howe, V.A. Fernandes, O. Gasnault, D.J.
745 Lawrence, S.S. Russell, M.A. Wieczorek, and B.H. Foing, *Planetary and Space Science* 57, 744 (2009).



This is the author's peer reviewed, accepted manuscript. However, the online version of record will be different from this version once it has been copyedited and typeset.

PLEASE CITE THIS ARTICLE AS DOI: 10.1063/5.0009830

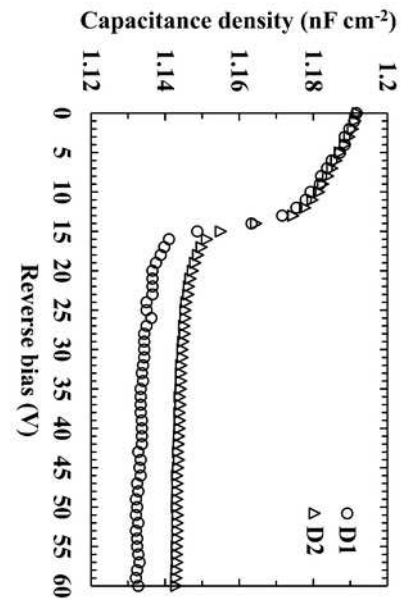


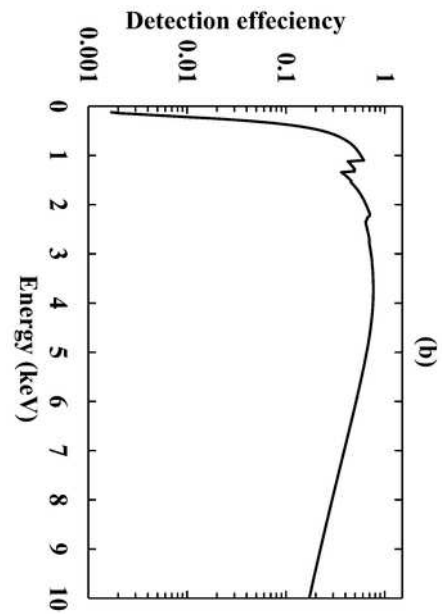
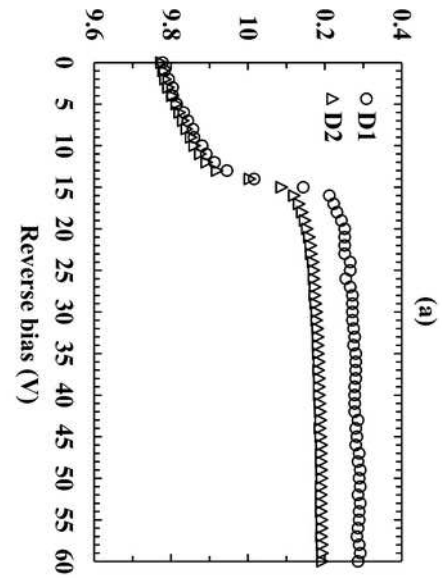




This is the author's peer reviewed, accepted manuscript. However, the online version of record will be different from this version once it has been copyedited and typeset.

PLEASE CITE THIS ARTICLE AS DOI: 10.1063/5.0009830

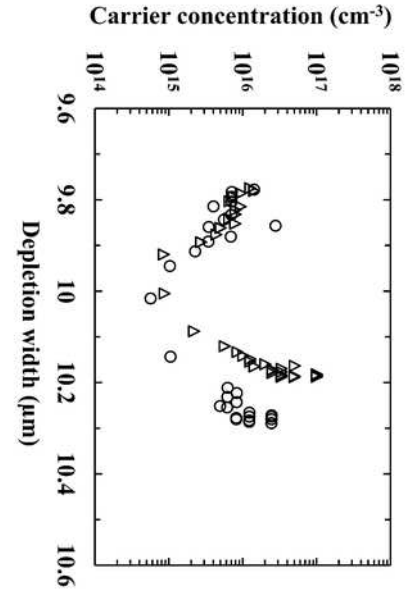






This is the author's peer reviewed, accepted manuscript. However, the online version of record will be different from this version once it has been copyedited and typeset.

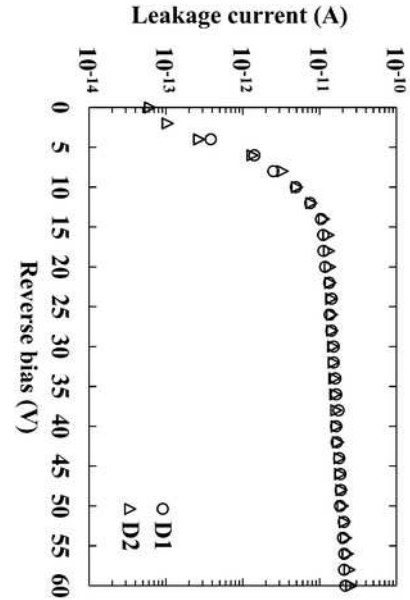
PLEASE CITE THIS ARTICLE AS DOI: 10.1063/5.0009830





This is the author's peer reviewed, accepted manuscript. However, the online version of record will be different from this version once it has been copyedited and typeset.

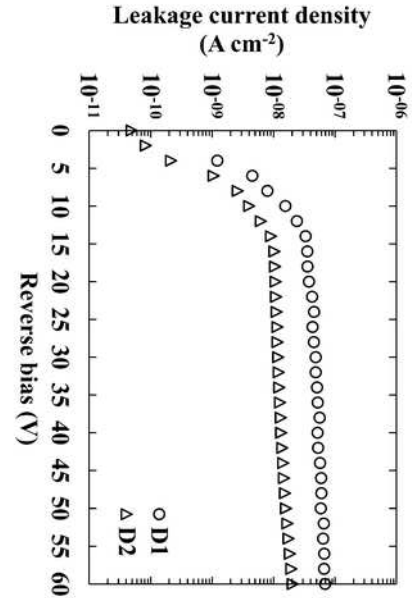
PLEASE CITE THIS ARTICLE AS DOI: 10.1063/5.0009830

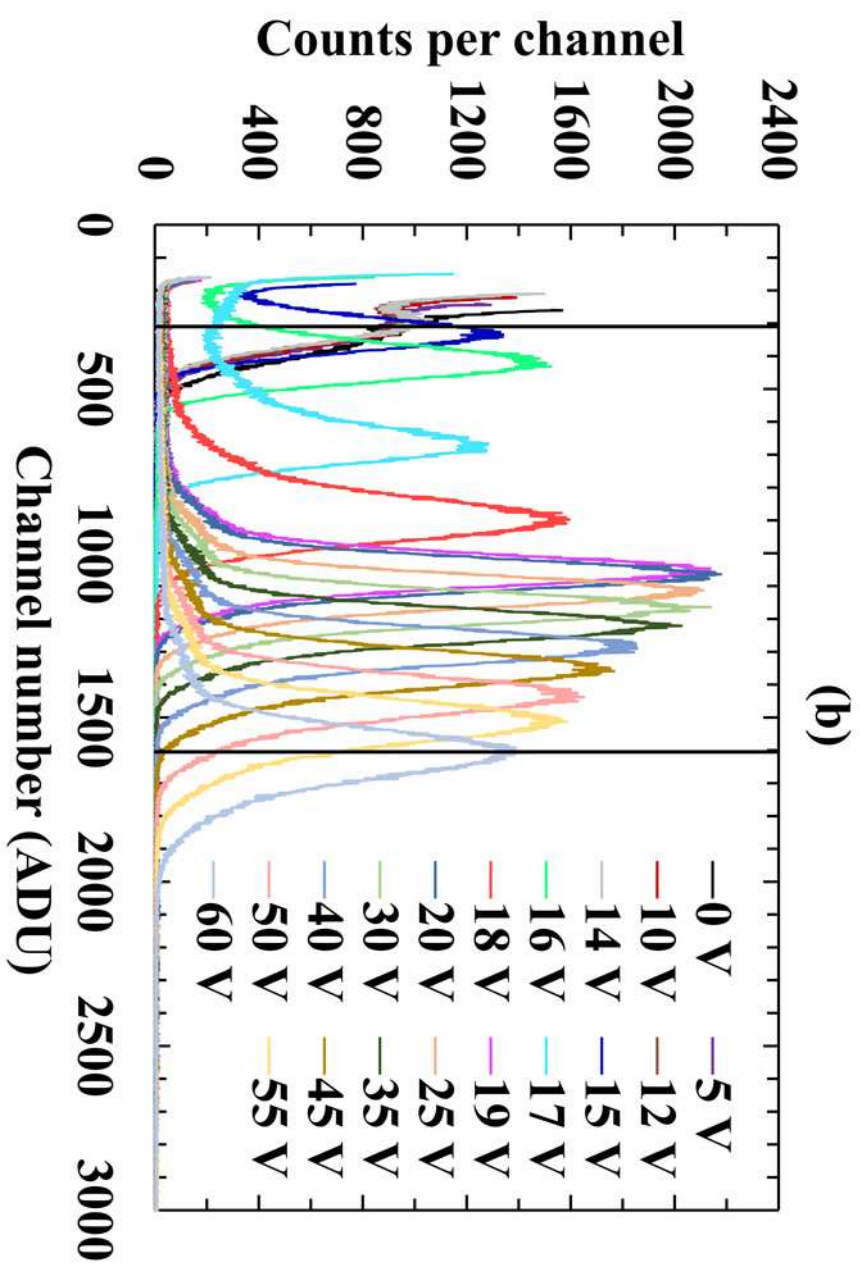
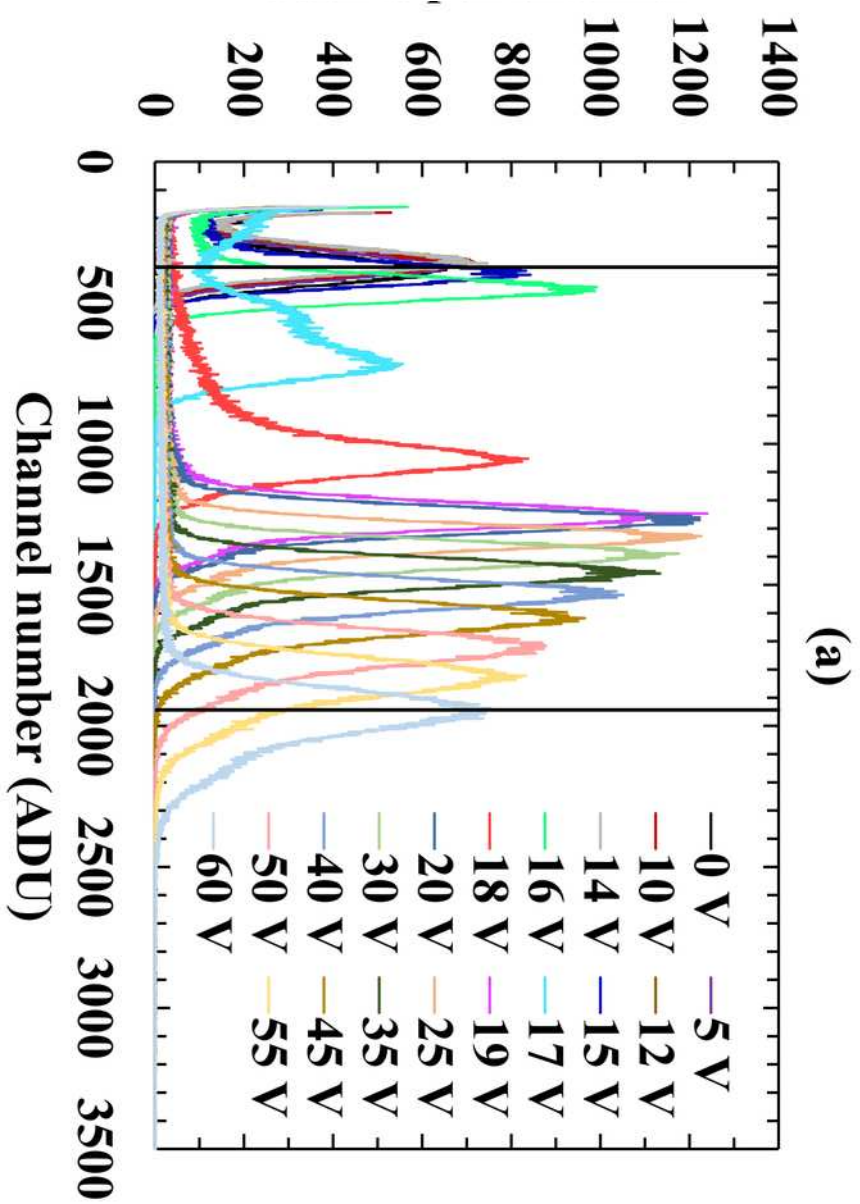




This is the author's peer reviewed, accepted manuscript. However, the online version of record will be different from this version once it has been copyedited and typeset.

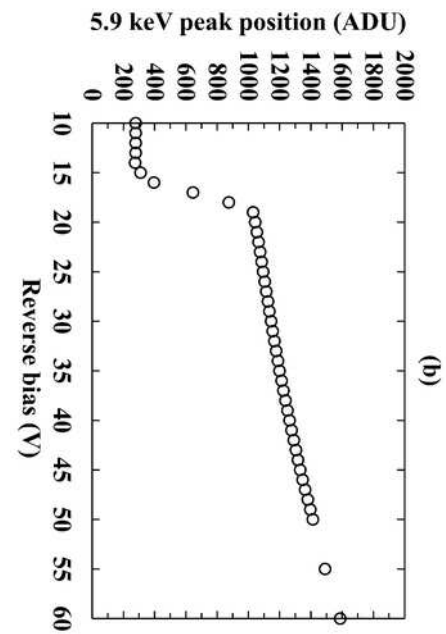
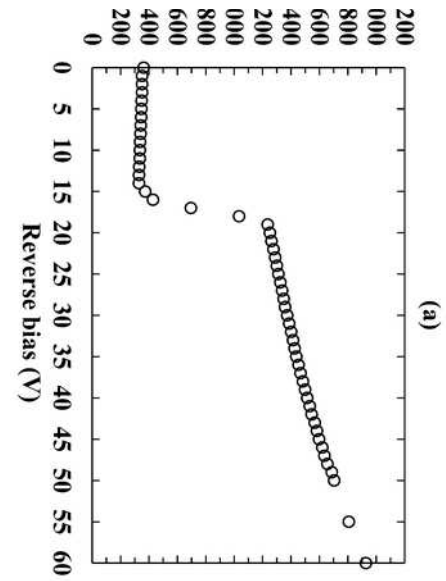
PLEASE CITE THIS ARTICLE AS DOI: 10.1063/5.0009830





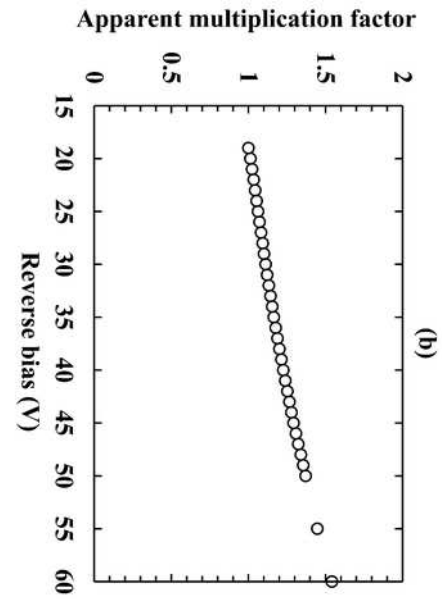
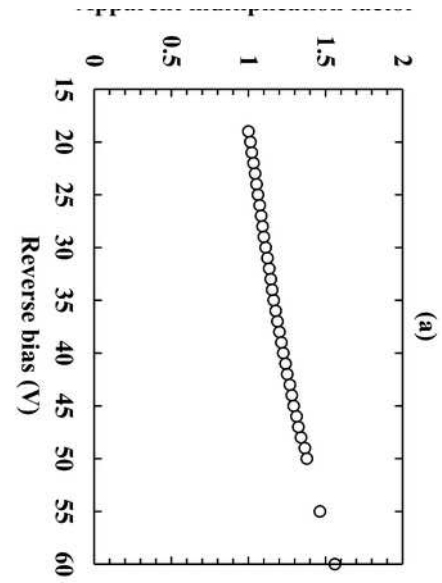
This is the author's peer reviewed, accepted manuscript. However, the online version of record will be different from this version once it has been copyedited and typeset.

PLEASE CITE THIS ARTICLE AS DOI: 10.1063/5.0009830



This is the author's peer reviewed, accepted manuscript. However, the online version of record will be different from this version once it has been copyedited and typeset.

PLEASE CITE THIS ARTICLE AS DOI: 10.1063/5.0009830



This is the author's peer reviewed, accepted manuscript. However, the online version of record will be different from this version once it has been copyedited and typeset.

PLEASE CITE THIS ARTICLE AS DOI: 10.1063/5.0009830

